RESEARCH

Tl(I) sequestration by pharmacosiderite supergroup arsenates: synthesis, crystal structures and relationships in Tl(I)–M(III)–As(V)–H$_2$O (M = Al, Fe) system

Tamara Đorđević[1] · Tarik Karasalihović[1] · Michael Stöger-Pollach[2] · Ljiljana Karanović[3]

Abstract

Due to their heteropolyhedral 3D open framework with cation exchange possibilities, pharmacosiderite supergroup arsenates play an essential role in the retention, mobility, and fate of various trace elements in the environment. However, the geochemical interaction with extremely toxic thallium (Tl) remains understudied. The formation of the compounds in the Tl(I)–M(III)–As(V)–H$_2$O (M(III) = Al, Fe) system results in the occurrence of poorly-crystalline thalliumpharmacosiderite, which was reported in the mining-impacted areas as well as in corresponding sediments and soils. Unfortunately, due to its low crystallinity, just a partial understanding of its key structural and compositional properties exists. Therefore, using hydrothermal synthesis (stainless steel autoclaves, autogenous pressure, T$_{max}$ = 170 °C), we have synthesized good-quality synthetic analogue of thalliumpharmacosiderite (Tpsd), Tl$_{2.5}$Fe$_4$[(AsO$_4$)$_3$(OH)$_4$](OH)$_{1.5}$·3H$_2$O, and still-not discovered "thalliumpharmacoalumite" (Tpal), Tl$_{1.25}$Al$_4$[(AsO$_4$)$_3$(OH)$_4$](OH)$_{0.25}$·4H$_2$O single crystals. They were characterized using single-crystal X-ray diffraction (SC-XRD), powder X-ray diffraction (PXRD), Raman spectroscopy, scanning electron microscopy (SEM) with energy dispersive spectroscopy (EDS) and transmission electron microscopy (TEM), providing more details on their chemical composition and crystal structure, thus bringing us one step further in better understanding of their structural and chemical properties and how they may relate to their formation in nature. Furthermore, Tl$_3$AsO$_4$ was resynthesized and its crystal structure and Raman spectrum were discussed, since it has a potential to be found in natural environments. Additionally, chemical characterization and Raman spectrum of a novel Tl-Fe-arsenate (Tl:Fe:As = 1:1:1) was mentioned. Consequently, the present research delivers useful insights on the role of pharmacosiderite supergroup arsenates in the environmental cycle of Tl.

Keywords Thallium · Pharmacosiderite supergroup arsenates · Thalliumpharmacosiderite · Crystal structure · Tl retention in minerals

Introduction

Thallium (Tl) can exhibit a high potential cytotoxicity and genotoxicity to humans and animals in its two main oxidation states (I and III) (Rodríguez-Mercado et al. 2019 and

✉ Tamara Đorđević
  tamara.djordjevic@univie.ac.at

1   Institut für Mineralogie und Kristallographie, Universität Wien, Josef-Holaubek-Platz 2, 1090 Wien, Austria

2   University Service Centre for TEM, Technische Universität Wien, Wiedner Hauptstr. 8-10, 1040 Wien, Austria

3   Laboratory of Crystallography, Faculty of Mining and Geology, University of Belgrade, Đušina 7, 11000 Belgrade, Serbia

references therein). Its concentration in water and soil is legally regulated in many countries but has an irreplaceable role in several high-tech fields and thus is present in selected e-waste of electrical and electronic equipment (Willner et al. 2021). It is generally introduced into the environment by mining, mineral processing, and metallurgy related to Tl-bearing deposits. Numerous discoveries of the new Tl-minerals (oxides, oxysalts, sulfides, tellurides, sulfosalts) and Tl-containing mineralisations in recent years (Voegelin et al. 2015; D'Orazio et al. 2017; Biagioni et al. 2017; Herrmann et al. 2018; Lin et al. 2020; Đorđević et al. 2021a, b; Gołębiowska et al. 2021; Voudouris et al. 2021; Kasatkin et al. 2022; Manceau et al. 2022) suggest that the risk of Tl exposure is much higher than documented, and the potential Tl pollution associated with the mining activities has attracted considerable attention.

In the weathering zones of the areas affected by mining, in soil horizons lacking secondary Tl-bearing minerals, Tl(I) adsorption onto micaceous phyllosilicates (mostly illite) (Martin et al. 2018; Wick et al. 2018; Voegelin et al. 2022), followed by Tl(I) and Tl(III) adsorption onto Mn-oxides was identified as the dominant Tl retention mechanism (Wick et al. 2019, 2020). However, in Tl-extreme environments, when illite and Mn-oxides are either absent or exhausted, Tl may be incorporated in the crystal structure of secondary Tl minerals. These are mainly Tl-bearing arsenates and sulfates (George et al. 2019; Đorđević et al. 2021a).

There are only very few secondary Tl-minerals, which may act as potential Tl sinks: dorallcharite ($TlFe^{3+}_3(SO_4)_2(OH)_6$) and other Tl-bearing jarosite-group minerals ($AFe_3(SO_4)_2(OH)_6$, $A = K$, Na, Ag, Pb), avicennite (Tl_2O_3) and thallium-pharmacosiderite ($TlFe_4[(AsO_4)_3(OH)_4]\cdot 4H_2O$) (Herrmann et al. 2018; Aguilar-Carrillo et al. 2020; Garrido et al. 2020; Đorđević et al. 2021a, b). Additionally, pharmacosiderite-group arsenate minerals are also considered as excellent sinks of arsenic (As). These minerals occur as minor compounds and are mostly tiny and often not-well crystalline. Their occurrence could be linked to slow weathering under circumneutral conditions (Majzlan et al. 2019). Hence, even at sites where substantial acidity is developed, pharmaco-siderite could crystallize in microenvironments that are able to neutralize that acidity (Vignola et al. 2018). On the other hand, the localities, where thalliumpharmacosiderite was confirmed are rare. Up to date, there are only two such localities worldwide: Allchar deposit in North Macedonia (Đorđević et al. 2021a) and Vorontsovskoe gold deposit (Northern Urals) in Russia (Kalinin and Savchenko 2019). Understanding the formation of the secondary Tl and As minerals begins with the examination of their crystal structures, which helps to locate the smallest crucial unit vital for the mineralization process. Thus, the aim of this paper is the synthesis and the complete characterization of "thalliumpharmacosiderite" (Tpsd, according to the mineral abbreviations given by Warr 2021) and its aluminum analogue "thalliumpharmacoalumite" (Tpal, by analogy), where Al^{3+} replaces Fe^{3+}. Therefore, Tpsd and Tpal have been hydrothermally synthesized and characterized using SC-XRD, SEM with EDS, TEM (EDS, EELS: electron-energy loss spectroscopy and SAED: selected area electron diffraction), as well as with micro-Raman spectroscopy. The results of our work are meant to give a more complete picture of "thalliumpahrmacosiderite" at the micro- and partly nano-scale for the user community to be able to employ in their respective work where such Tl–Fe(III)–arsenates are often encountered. Furthermore, crystal structure and Raman spectrum of synthetic Tl_3AsO_4 was discussed, since it has potential to be found in natural environments. Although its structure had already been described, we decided to include Tl_3AsO_4 in this paper since it was obtained by slightly different synthetic route than reported previously (Effenberger 1998), its unit cell has different origin and orientation and the redetermination reveals more precise results compared to the previous refinement, i.e. a somewhat higher accuracy in terms of bond lengths and angles. In addition, a novel Tl-Fe-arsenate with Tl:Fe:As ~ 1:1:1 will be briefly described.

Experimental

Preparation of the single-crystals

Synthetic Tpsd and Tpal have been obtained using low-temperature hydrothermal method. The following reagents were used in stoichiometric quantities: $FeCl_3\cdot 6H_2O$ (Merck > 99%), $FeNO_3$ (Fluka > 98%), As_2O_5 (Alfa Aesar, ultra-pure), Tl_2CO_3 (Fluka > 99.9%), Tl_2NO_3 (Merck > 99%), Tl_2SO_4 (Fluka > 98%), $AlCl_3\cdot 6H_2O$ Merck (> 99%) and $Al_2(SO_4)_3\cdot 18H_2O$ (Merck, cryst. pure).

The synthesis protocol of Tpsd was adapted from previously reported by Majzlan et al. (2019). The experimental setup of growing Na-, K-, Sr- and Ba-dominant members of pharmacosiderite group was supplemented with Tl^+ as a dominant A^+ cation (or cation in the channels of the open-framework). Undeviating synthesis of Tl-pharmacosiderite succeeded, so the approach of ion exchange synthesis was not needed. However, the pH value was put more into consideration, with higher initial values (pH = 2–7) as described by Majzlan et al. (2019). Furthermore, different mass proportions were applied. Two rows of samples with different ferric components were prepared, yielding eleven samples in the first synthesis run. For the synthesis of Tpsd the mixtures of 0.1 g of Tl_2SO_4, 0.1 g of As_2O_5 and 0.5 g of $FeCl_3\bullet 6H_2O$ or $FeNO_3$, respectively, were prepared. The mixture dissolved in the 5 ml of deionized water developed a reddish-brown solution. The initially very low pH of 1 was adjusted with NaOH to the values varying between pH = 2–7, forming a milky ocher suspension. The mixtures were transferred into polytetrafluoroethylene vessels and filled with distilled water to the 80% of their inner volume. Subsequently, the mixtures were enclosed into stainless steel autoclaves and heated under autogenous pressure under the following heating and cooling conditions: the mixtures were heated from room-temperature to 170 °C (4 h), held at that temperature for 72 h, and cooled to room temperature (44 h). The reaction products were filtered and washed several times using distilled water. Tpsd crystallized as transparent orange cubes up to 15–65 μm in length (Fig. 1a).

The experimental setup for the synthesis of Tpal was identical to the synthesis of Tpsd. We used two different Al-salts, $Al_2(SO_4)_3$ and $AlCl_3$ as the Al-sources. The mass proportions of the reactants were taken from the most successful syntheses-runs of Tpsd. The initial pH values were

Fig. 1 White-light photomicrographs of the single crystals and crystal aggregates of (**a**) Tpsd, $Tl_{2.5}Fe_4[(AsO_4)_3(OH)_4]$ $(OH)1.5\cdot3H_2O$, (**b**) Tpal, $Tl_{1.25}Al_4[(AsO_4)_3(OH)_4]$ $(OH)_{0.25}\cdot4H_2O$, (**c**) Tl_3AsO_4 and (**d**) novel Tl-Fe-arsenate with Tl:Fe:As ~ 1:1:1
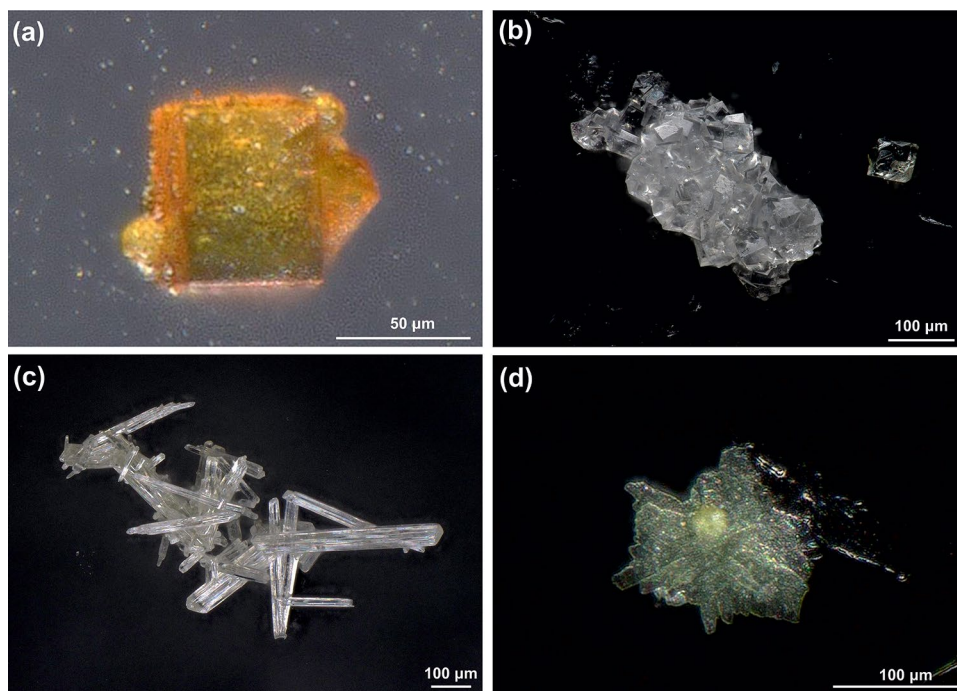
adjusted using NaOH and were ranging from 4 to 7. The mixtures were transferred into polytetrafluoroethylene vessels and filled with distilled water to the 80% of their inner volume. Subsequently, they were enclosed into stainless steel autoclaves and heated under autogenous pressure under the following heating and cooling conditions: the mixtures were heated from room-temperature to 170 °C (4 h), held at that temperature for 72 h, and cooled to room temperature (99 h). The reaction products were filtered and washed several times using distilled water. Tpal crystallized as transparent colorless cubes up to 15–40 μm in length (Fig. 1b). The synthesis of Tpal was successful in two of five synthesis-runs. Tpal forms colorless transparent cubes (mostly aggregated) up to 10–35 μm. Besides Tpsd, Tpal and Tl_3AsO_4 the fourth unknown phase (Fig. 1d) (previously only found in one sample) was predominantly synthesized with larger crystal size. The micaceous crystal habitus and twinning proved to be difficult for SC-XRD sample preparation, but we managed to identify this compound using SEM–EDS analyses and Raman spectroscopy as Tl-Fe-arsenate, with Tl:Fe:As ~ 1:1:1.

In a study on the natural Tl- and As-rich samples Đorđević et al. (2021a) have detected intensive Tl uptake by previously unknown Tl-arsenate phases (with Tl:As ratios ~ 2 and 4), spotted in the carbonate-buffered (near-neutral pH) As- and Tl-rich technosols and waste dumps. As the crystallinity of these phases was poor, their crystal structure remained unknown, but we managed to successfully record their Raman spectra. The information on their crystal structure would surely be valuable for the analyses of their stability in the natural systems. Therefore, we have conducted further

synthesis committed to the preparation of the Tl-arsenate with Tl:As ratios ranging from 2:1 to 4:1. The initial pH values were varied from 6 to 8 mimicking the natural conditions in the carbonate-buffered environments. A total of ten samples were prepared, each five with either Tl_2CO_3 or Tl_2SO_4 as the starting reagents. Approximately 0.1 g of Tl_2CO_3, or Tl_2SO_4 respectively, was mixed with 0.02 g of As_2O_5 and diluted in 2.5 ml of distilled H_2O. The carbonaceous solution had an initial pH of 7.5, the solution containing sulfate, SO_4^{2-} anions was adjusted with NaOH to pH = 6–8. The mixtures were transferred into polytetrafluoroethylene vessels and filled with distilled water to the 80% of their inner volume. Subsequently, they were enclosed into stainless steel autoclaves and heated under autogenous pressure under the following heating and cooling conditions: the mixtures were heated from room-temperature to 200 °C (4 h), held at that temperature for 72 h, and cooled to room temperature (44 h). After the cooling, the pH values were measured as 6–9. The reaction products were filtered and washed several times using distilled water. The synthesis-products resulted in monophaseous Tl_3AsO_4, already described by Effenberger (1998). It crystallized as colorless, transparent needles up to 7 mm in length (Fig. 1c) with vitreous luster and vertical striations, sometimes radially aggregated.

Scanning electron microscopy

Qualitative chemical analyses were performed using a JEOL JSM-6610 LV SEM with W-filament (15 kV, working distance 17 mm), equipped with secondary electrons (SE) and

back-scattered electron (BSE) detector and electron back-scatter diffraction (EBSD) and cathodoluminescence units. The investigated single crystals were fixed with conducting carbon onto Al-sample holders and were consequently coated with a thin layer of carbon for chemical analysis. EDS analysis proved the presence of each reported element in the Tpsd, Tpal, Tl_3AsO_4 and in Tl-Fe-arsenate.

Transmission electron microscopy

For TEM analysis, lamellae were prepared by employing focused ion beam (FIB) using a ThermoFisher Scios II dual beam FIB. The lamellae were then directly transferred into a FEI TECNAI G20 TEM equipped with a GATAN GIF 2001 image filter and energy-loss spectrometer and an EDAX-AMETEC Octane T Elite plus EDS detector. EELS-data were used for determining the oxidation state of Fe within the Tpsd crystals. For this purpose the energy loss near edge structure (ELNES) of the Fe-$L_{3,2}$ ionisation edge was measured *via* EELS. The collection angle used was 4.03 mrad. For the determination of the Fe L_3/L_2 ratio the method introduced in van Aken and Liebscher (2002) was employed. Selected area diffraction was recorded using the GATAN Orius 600 charge-coupled device (CCD) camera.

Single crystal X-ray diffraction analysis

Suitable single crystals of Tpsd, Tpal and Tl_3AsO_4 were selected and glued to the thin glass fibers. The crystals, which exhibited sharp reflection spots, were chosen for data collection. For Tpal and Tl_3AsO_4 data collection was performed on a Nonius KappaCCD single-crystal four-circle diffractometer (Mo tube, graphite monochromator, CCD detector frame size: 621×576 pixels, binned mode), equipped with a 300 μm diameter capillary optics collimator. A complete sphere of reciprocal space (φ and ω scans) was measured at room temperature. The intensity data were processed with the Nonius program suite DENZO-SMN (Nonius 2005–2007), corrected for Lorentz, polarization, and background effects and, by the multi-scan method (Otwinowski et al. 2003), for absorption. A single crystal of Tpsd was studied on a Bruker X8 Kappa APEX II CCD diffractometer, equipped with a monocapillary optics collimator and graphite-monochromatised Mo$K\alpha$ radiation. The single-crystal data of Tpsd were collected at ambient conditions, integrated and corrected for Lorentz and polarization factors and absorption corrected by scaling of partial multi-scans. The intensity data were processed with the Bruker-Nonius programme suite SAINT-Plus (Bruker 2007).

Both structures of Tpsd and Tpal were solved in the cubic space group $P\bar{4}3m$ (No. 215), while the crystal structure of Tl_3AsO_4 was solved in hexagonal space group $P6_3$ (No. 173) by direct methods using SHELXT (Sheldrick 2015a) and

refined on F^2 by full-matrix least-squares using SHELXL version 2018/3 (Sheldrick 2015b) and WinGX (Farrugia 2012). The "absolute structure" for the non-centrosymmetric structures was also determined and confirmed by the Flack parameter calculation. When the full-matrix least-squares refinement on F^2 (Sheldrick 2015b) involving anisotropic displacement parameters for all non-hydrogen atoms converged to an agreement index $R1$ less than 0.1, the Flack parameter x (Flack 1983; Parsons et al. 2013) was near to unity and atomic coordinates were inverted to get the correct absolute structure. This lowered the Flack parameter x and it dropped to 0.04(2) in Tl_3AsO_4 and 0.035(13) in Tpal (Table 1). The crystal structure of Tl_3AsO_4 is in very good agreement with the already described one (Effenberger 1998), but the unit cell of Tl_3AsO_4 differs in its origin and orientation within the structure.

Crystal data, information on the data collection and results of the final structure refinement are compiled in Table 1. The fractional atomic coordinates, occupancies and equivalent or isotropic atomic displacement parameters are given in Table 2 and anisotropic atomic displacement parameters in Table S1 in the supplementary file. Selected bond distances (Å) with hydrogen bonds are presented in Table 3. The molecular graphics were done with ATOMS (Dowty 2000) and VESTA-3.2.1 (Momma and Izumi 2011).

Raman spectroscopy

For the detailed study of the arsenate groups, single-crystal Raman spectra of Tpsd, Tpal and Tl_3AsO_4 were measured with a Horiba LabRam–HR system equipped with Olympus BX41 optical microscope in the spectral range between 100 and 4000 cm^{-1}. The 632.8 nm excitation line of a He–Ne laser was focused with a $100\times$ objective (N.A. = 0.90) on the randomly oriented single crystal. The nominal exposure time of the acquired spectra was 10 s (confocal mode, Olympus 1800 lines/mm, 1.5 μm lateral resolutions, and approximately 3 μm depth resolution). The density of the laser power was well below the threshold for possible sample changes due to intense laser-light absorption and resulting temperature increase.

Results and discussion

Crystal chemistry and structural properties of Tpsd and Tpal

SEM–EDS analysis of Tpsd (Fig. 2a) revealed the presence of Tl in the range of 5.7–5.9 at%, Fe in the range of 13.9–17.1 at% and As in the range of 11.7–12.3 at%. Atomic proportions of the main elements calculated from atomic %, Tl:Fe:As = 1.5:3.8:3 correspond not fully with the ratio

Table 1 Crystal data, data collection and refinement details for Tpsd, Tpal and Tl_3AsO_4

	Tpsd	**Tpal**	**Tl_3AsO_4**
Crystal data			
Chemical formula	$As_3H_{11.50}Fe_4O_{20.50}Tl_{2.50}$	$Al_4H_{12.25}As_3O_{20.25}Tl_{1.25}$	AsO_4Tl_3
Formula weight M_r	1298.68	924.49	752.03
Crystal system, space group	Cubic, $P\bar{4}3m$	Cubic, $P\bar{4}3m$	Hexagonal, $P6_3$
Temperature (K)	298	298	298
a, b, c (Å)	$a = 7.9645(1)$	$a = 7.7281(4)$	$a = 8.5259(12)$ $c = 5.238(1)$
V (Å^3)	505.21(2)	461.55(7)	329.74(11)
Z	1	1	2
Radiation type	Mo $K\alpha$ radiation	Mo $K\alpha$ radiation	Mo $K\alpha$ radiation
μ(mm^{-1})	27.62	16.55	78.03
Crystal size (mm)	$0.05 \times 0.05 \times 0.05$	$0.03 \times 0.03 \times 0.03$	$0.02 \times 0.02 \times 0.10$
Crystal habit, color	cubic, orange	cubic, clorless	needle-like, colorless
Data collection			
Diffractometer	Bruker X8 Kappa APEX II CCD	Nonius Kappa CCD	Nonius Kappa CCD
Absorption correction	Multi-scan	Multi-scan	Multi-scan
θ range for data collection (°)	$2.6 - 29.9$	$2.6 - 30.0$	$2.8 - 30.5$
h,k,l—range	$-11{:}11, -11{:}11, -11{:}11$	$-10{:}10, -7{:}7, -7{:}7$	$-12{:}12, -12{:}12, -7{:}7$
No. of measured, independent and observed $[I > 2\sigma(I)]$ reflections	20718, 318, 314	462, 296, 283	4080, 688, 640
R_{int}	0.030	0.015	0.046
$(\sin \theta/\lambda)_{max}$ (Å^{-1})	0.702	0.703	0.713
Refinement			
$^aR[F^2 > 2\sigma(F^2)]$, $^{b,c}wR(F^2)$, ^dS	0.016, 0.043, 1.17	0.025, 0.065, 1.13	0.021, 0.055, 1.12
^{c}weighting parameters g_1, g_2	0.0152, 1.3239	0.033, 0.750	0.0306, 0.5202
^{e}Extinction coefficient	0.0045(8)	0.002(2)	0.0031(4)
No. of reflections	318	296	688
No. of parameters	31	28	26
No. of restraints	4	4	1
H-atom treatment	*H-atom parameters constrained	*H-atom parameters constrained	/
$\Delta\rho_{max}$, $\Delta\rho_{min}$ (eÅ^{-3})	0.56, -0.34	1.17, -0.77	1.94, -1.43
Absolute structure	^{f}Flack x determined	^{g}Flack x determined	^{h}Flack x determined
Absolute structure parameter x	0.015(8)	0.035(13)	0.04(2)

*The water H atoms were refined using DFIX distance restraints with O—H = 0.85 Å, H1—H2 = 1.37 Å and $U_{iso}(H) = 1.5U_{eq}(O)$

$^aR = \Sigma[\,||F_o| - |F_c|\,|]/\Sigma|F_o|$

$^bwR = \{\Sigma[w(F_o^2 - F_c^2)^2]/\Sigma[w(F_o^2)^2]\}^{1/2}$

$^cw = 1/[\sigma^2(F_o^2) + (g_1P)^2 + g_2P]$ where $P = (F_o^2 + 2F_c^2)/3$

$^d S = \{\Sigma[w(F_o^2 - F_c^2)^2]/(N_{obs} - N_{param})\}^{1/2}$

$^eF_c^* = kF_c[1 + 0.001xF_c^2\lambda^3/\sin(2\theta)]^{-1/4}$ where k is the overall scale factor (SHELXL)

^{f}Flack x determined using 123 quotients $[(I+)-(I-)]/[(I+)+(I-)]$

^{g}Flack x determined using 111 quotients $[(I+)-(I-)]/[(I+)+(I-)]$

^{h}Flack x determined using 274 quotients $[(I+)-(I-)]/[(I+)+(I-)]$; (Parsons et al. 2013)

of Tl:Fe:As = 2.5:4:3 obtained from the structural analyses. Chemical analysis of Tpal (Fig. 2b) revealed the presence of Tl in the range of 4.7–5.1 at%, aluminum in the range of 17.2–17.4 at% and As in the range of 13.2–13.3 at%. Atomic proportions of main elements calculated from atomic %, Tl:Al:As = 1.1:3.9:3 correspond very well with the ratio of Tl:Al:As = 1.2:4:3 obtained from the structural analyses. Chemical analysis of Tl_3AsO_4 (Fig. 2c) revealed the presence of 13.0 at% of Tl, and 36 at% of As, yielding the atomic proportions of main elements calculated from

Table 2 Fractional atomic coordinates, occupation factors and isotropic or equivalent isotropic displacement parameters (Å^2) in Tpsd, Tpal and Tl_3AsO_4

Space group $P\overline{4}3m$

Atom	Site	xyz	Tpsd $Tl_{2.5}Fe_4[(AsO_4)_3(OH)_4](OH)_{1.5}\cdot 3H_2O$				Tpal $Tl_{1.25}Al_4[(AsO_4)_3(OH)_4](OH)_{0.25}\cdot 4H_2O$			
			x	z	occ. (<1)	U_{iso}^*/U_{eq}	x	z	occ. (<1)	U_{iso}^*/U_{eq}
M(III)	4e	xyz	0.14276(8)	0.14276(8)		0.0052(2)	−0.1398(3)	−0.1398 (3)		0.0144(7)
As	3d	½,0,0	0.5	0.0		0.0075(2)	0.5	0.0		0.0145(3)
O1	12i	xxz	0.1257(3)	0.3848(4)		0.0125(7)	−0.1268(5)	−0.3764(4)		0.0171(9)
O2	4e	xxx	−0.1156(4)	−0.1156(4)		0.0069(12)	0.11426(6)	0.11426(6)		0.0136(17)
H2	4e	xxx	−0.176(2)	−0.176(2)		0.010*	0.177(2)	0.177(2)		0.021*
Tl1a	3c	0,½,½	0.0	0.5	0.1667	0.070(3)	0.0	0.5	0.4166	0.0817(8)
Tl1b	6g	x,½,½	0.0578(3)	0.5000	0.3333	0.04552(5)	/	/	/	/
O4a	4e	xxx	−0.3076(13)	−0.3076(13)	0.56(2)	0.071(5)	0.3119(16)	0.3119(16)	0.72(4)	0.074(6)
O4b	4e	xxx	−0.3941(18)	−0.3941(18)	0.44(2)	0.071(5)	0.352(4)	0.352(4)	0.28(4)	0.074(6)
O5	1b	½,½,½	0.5	0.5	0.5	0.014(4)	0.5	0.5	0.25	0.025(12)
H5	4e	xxx	−0.438(2)	−0.438(2)	0.125	0.022*	0.436(2)	0.436(2)	0.0625	0.038*

Space group $P6_3$ Tl_3AsO_4

atom	site	xyz	x	y	z	U_{iso}^*/U_{eq}
Tl	6c	xyz	0.64479(4)	0.90808(4)	0.5688(3)	0.02608(16)
As	2b	⅓,⅔,z	0.333333	0.666667	0.0826(5)	0.0170(3)
O1	2b	⅓,⅔,z	0.333333	0.666667	0.413(2)	0.024(3)
O2	6c	xyz	0.5197(12)	0.1220(10)	0.4843(16)	0.0301(18)

Table 3 Selected bond lengths and bond-valences in Tpsd, Tpal and Tl_3AsO_4

| Tpsd M–O bond (Å)		$\Sigma\nu_i$ (v.u.)	Tpal M–O bond (Å)		$\Sigma\nu_i$ (v.u.)	Tl_3AsO_4 M–O bond (Å)		$\Sigma\nu_i$ (v.u.)*
Fe1—O1	1.937(4) 3×	0.618 3×	Al1—O1	1.834 (5) 3×	0.610 3×	/	/	/
Fe1—O2	2.080(3) 3×	0.420 3×	Al1—O2	1.983 (4) 3×	0.408 3×	/	/	/
CN=6	<Fe–O>=2.009	$\Sigma\nu_i$=3.112	CN=6	<Al–O>=1.909	$\Sigma\nu_i$=3.053	/	/	/
Sum of e. i. radii	0.645+1.4=2.045			0.535+1.4=1.935		/	/	/
As1—O1	1.687(4) 4×	1.241 4×	As1—O1	1.683(4) 4×	1.254 4×	As1—O1	1.731(13)	1.1022
						As1—O2	1.681(7) 3×	1.2617 3×
CN=4	<As–O>=1.685	$\Sigma\nu_i$=4.964	CN=4	<As–O>=1.684	$\Sigma\nu_i$=5.018	CN=4	<As–O>=1.6935	$\Sigma\nu_i$=4.89
Sum of e. i. radii	0.335+1.4=1.735			0.335+1.4=1.735			0.335+1.4=1.735	
Tl1a—O4a	3.271(2) 0.56×4	0.0450 0.56×4	Tl1—O4a	3.168(2) 0.72×4	0.0595 0.72×4	Tl1—O2^i	2.532(8)	0.3320
Tl1a—O4b	3.358(6) 0.44×4	0.0356 0.44×4	Tl1—O4b	3.166(5) 0.28×4	0.0598 0.28×4	Tl1—O1	2.547(4)	0.3188
Tl1a—O1	3.2761(17) 8×	0.0444 8×	Tl1—O1	3.192(2) 8×	0.0558 8×	Tl1—O2	2.570(9)	0.2996
CN=2+2+8	<Tl–O>=3.287	$\Sigma\nu_i$=0.5187	CN=3+1+8	<Tl–O>=3.184	$\Sigma\nu_i$=0.6847		<Tl–O>=2.550	$\Sigma\nu_i$=0.9504
Tl1b—O4a	2.942(4) 0.56×2	0.1096 0.56×2	/	/	/	Tl1—O2^{ii}	3.324(9)	0.0390
Tl1b—O4b	2.932(5) 0.44×2	0.1126 0.44×2	/	/	/	Tl1—O2^{iii}	3.508(8)	0.0237
Tl1b—O1	3.166(2) 4×	0.0598 4×	/	/	/	Tl1—O 7×	3.628(9)-4.942(8)	$\Sigma\nu_i$=0.0468
CN=1+1+4	<Tl–O>=3.090	$\Sigma\nu_i$=0.461	/	/	/	CN=3+2	<Tl–O>=2.896	$\Sigma\nu_i$=1.0131
Tl1b—O4a	3.629(2) 0.56×2	0.0195 0.56×2	/	/	/	CN=3+2+7	<Tl–O>=3.688	$\Sigma\nu_i$=1.0599
Tl1b—O4b	3.792(8) 0.44×2	0.0125 0.44×2	/	/	/	/	/	/
Tl1b—O1	3.445(2) 4×	0.032 4×	/	/	/	/	/	/
CN=1+1+4	<Tl–O>=3.530	$\Sigma\nu_i$=0.161	/	/	/	/	/	/
CN=2+2+8	<Tl–O>=3.310	$\Sigma\nu_i$=0.622	/	/	/	/	/	/
Tl1a—O5	3.9823(1) 2×	0.0066 2×	Tl1—O5	3.8640(2) 2×	0.0091 2×	O1: $\Sigma\nu_i$=1.1022+3*0.3188=2.0586		
Tl1b—O5	3.522(2) 2×	0.0229 2×	/	/	/	O2: $\Sigma\nu_i$=1.2617+0.3320+0.2996+0.0390+0.0237=1.9560		
/	/	$\Sigma\nu_i$=0.059	/	/	$\Sigma\nu_i$=0.018			
Sum of e. i. radii	1.7+1.4=3.1	/		1.7+1.4=3.1	/		1.7+1.4=3.1	/
O– H···O	O··· O	/	O–H···O	O··· O	/	/	/	/
O2—H2···O4a	2.648 (19)	/	O2—H2···O4a	2.65 (2)	/	/	/	/
O5—H5···O4a	2.655 (18)	/	O5—H5···O4a	2.52 (2)	/	/	/	/
splitting distance						Tl–Tl contact		
Tl1a– Tl1b	0.461 (3)	/	/	/	/	Tl–Tl	3.7778(5) 4×	/
Tl1b– Tl1b^i	0.922 (5)	/	/	/	/			/
O4a—O4b	1.21(3)	/	O4a—O4b	0.57 (5)	/			/
/	/	/	/	/	/	/		/
Symmetry codes: (i) -x+1, -y, z						*Symmetry codes:* (i) -x+1, -y+2, z+1/2; (ii) -x+1, -y+2, z-1/2; (iii) -x+y, -x+1, z		

atomic % to Tl:As = 1:1. Chemical analysis of the novel Tl-Fe-arsenate (Fig. 2d) revealed the presence of Tl in the range 15.0–15.9 at%, Fe in the range of 16.0–16.4 at%, and As in the range of 16.2–16.7 at%, yielding the atomic proportions of main elements calculated from atomic % to the ratio Tl:Fe:As = 1:1:1.

SC-XRD analysis showed that the crystal structures of $AFe_4(OH)_4(TO_4)_3 \cdot nH_2O$ (Tpsd) and $AAl_4(OH)_4(TO_4)_3 \cdot nH_2O$ (Tpal) are comparable to the other $AM_4(OH)_4(TO_4)_3 \cdot nH_2O$ structures of the pharmacosiderite and pharmacoalumite group of minerals. The fundamental building unit in all these structures contains $M_4(OH)_4O_{12}$ clusters of four edge-sharing $M(OH)_3O_3$-octahedra (Fig. 3a, b). They are interconnected by TO_4-tetrahedra, forming heteropolyhedral 3D open framework (Fig. 3c, d) with different exchangeable A cations, H_2O molecules and hydroxyl groups in available channels located at symmetry equivalent positions (x ½ ½), (½ y ½) and (½ ½ z).

The initial location of the framework atoms M(III) (= Fe^{3+} in Tpsd and Al^{3+} in Tpal), As, O1 and O2 in Tpsd and Tpal revealed that they were located in the similar positions to those reported earlier for the pharmacosiderite-type arsenates (Buerger et al. 1967; Hager et al. 2010): M and O2 are at special positions 4e, As is at special position 3d and O1 is at special position 12i. Positionally disordered Tl atoms in Tpsd were found from the difference Fourier map in a split

Fig. 2 SE-SEM images of (**a**) Tpsd, $Tl_{2.5}Fe_4[(AsO_4)_3(OH)_4]$ (OH)1.5·3H_2O, (**b**) Tpal, $Tl_{1.25}Al_4[(AsO_4)_3(OH)_4]$ (OH)$_{0.25}$·4H_2O, (**c**) Tl_3AsO_4 and (**d**) novel Tl-Fe-arsenate with Tl:Fe:As ~ 1:1:1
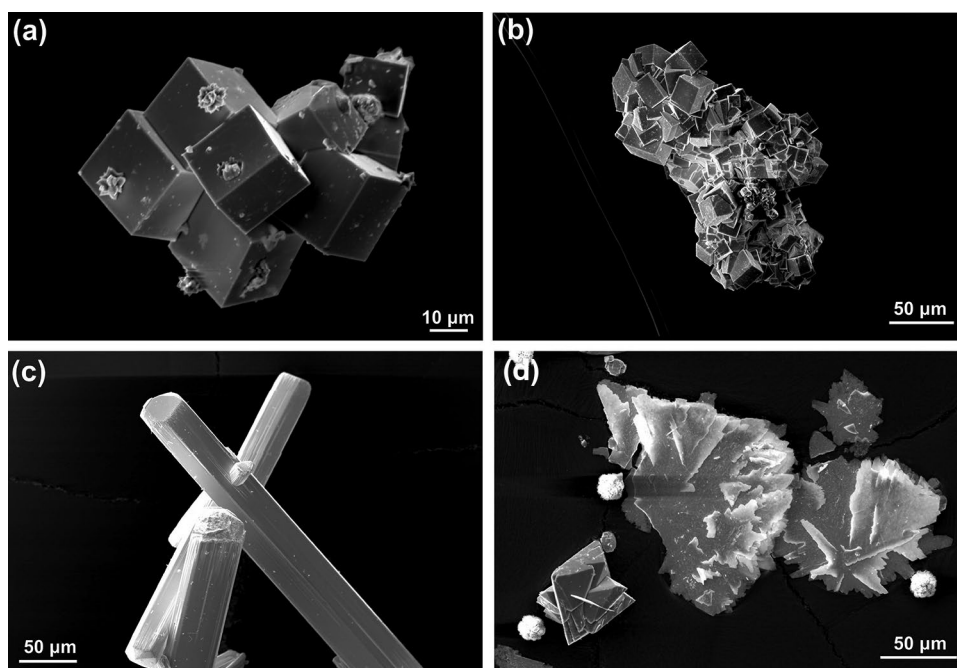
position, where one maximum was positioned at 3*c*, and the other near to it, at 6 *g*. In Tpal, a positional splitting of Tl atoms is not present and Tl is positioned exactly in 3*c* site (Table 2). However, large elongated ADP ellipsoids are found indicating the disordered arrangement of Tl atoms. Similar statistical disorder of different exchangeable cations was found in natropharmacosiderite and plumbopharmacosiderite (Hager et al. 2010; Vignola et al. 2018). In some minerals and synthetic compounds of the pharmacosiderite-type structure those sites are usually occupied by the O3 atoms from the H_2O molecules. Therefore, and for the convenience of comparison, atomic sites for the oxygen atoms situated in the channels of Tpsd and Tpal are named as O4 and O5, according to the notation given by Mills et al. (2010a, b). Structure refinements of Tpsd and Tpal show a strong positional disorder of the O4 atoms demonstrated by their large ADP ellipsoids and split positions, which are alternatively and not fully occupied. These sites denoted as O4a and O4b are both found at 4*e* positions (Table 2). They were attributed to O atoms of H_2O molecules or hydroxyl groups. Furthermore, there was a low residual in the difference map at 1*b* site which was attributed to another partially occupied oxygen site, O5. This final model converged to $R_1 = 0.015$ for Tpsd and yielded the formula $Tl_{2.5}Fe_4[(AsO_4)_3(OH)_4](OH)_{1.5}·3H_2O$, while the final model for Tpal, which was obtained in similar way, yielded the formula $Tl_{1.25}Al_4[(AsO_4)_3(OH)_4](OH)_{0.25}·4H_2O$ and $R_1 = 0.025$ (Table 1). The anisotropies were found to be only moderate except for Tl and oxygen atoms in the channels (O4 and O5) due to their positional disorder and partial occupancy. The displacement parameters of the O4b position were restrained to be the same as for the O4a position and the

sum of O4a + O4b was restrained to give a total occupancy of 1.00. Hydrogen atoms from H_2O molecules and hydroxyl groups were located in the difference-Fourier map and refined using DFIX distance restraints with O—H = 0.85 Å and $U_{iso}(H) = 1.5U_{eq}(O)$. Because of positional disorder of O4a and O4b, H-atoms bound to them are also highly disordered and it was not possible to locate precisely their positions. Therefore, these H-atoms were not included in the refinement.

The Fe(III) and Al(III) ions in Tpsd and Tpal, respectively, are in a nearly regular octahedral coordination $M(O2H2)_3O1_3$, while As(V) ion is tetrahedrally coordinated by four bridging O1 oxygen atoms (Table 3, Fig. 3). Each hydroxyl O2H2$^-$ group is shared by three *M*-atoms in $M_4(O2H2)_4O1_{12}$ clusters, which consists of four $M(O2H2)_3O1_3$- octahedra (Fig. 3a). The individual *M*—O1 bond lengths are 1.937(3) and 1.834(5) Å, while *M*—O2 bond lengths are 2.080(3) and 1.983(4) Å in Tpsd and Tpal, respectively (Table 3). The average Fe(III)—O and Al(III)—O distances (< 2.009 > and < 1.909 > Å in Tpsd and Tpal, respectively) are close to those calculated from the effective ionic radii (Shannon 1976) of six-coordinated Fe(III) (high spin) ions (0.645 + 1.38 = 2.025 Å) and Al(III) ions (0.535 + 1.38 = 1.915 Å) and CN = 4 for O1 (As, Fe or Al, two Tl) and O2 (H, three Fe or Al). They are also near to the reported average Fe—O and Al—O bond lengths of 2.015 and 1.903 Å (Gagné and Hawthorne 2018, 2020). The bond valence sum for Fe(III) and Al(III) are $\Sigma v_i = 3.11$ and $\Sigma v_i = 3.05$ v.u. suggesting that octahedral trivalent cations are well balanced (Table 3).

The adjacent $M_4(O2H2)_4O1_{12}$ are linked together by the corners of $AsO1_4$ tetrahedra (Fig. 3b). Six neighboring

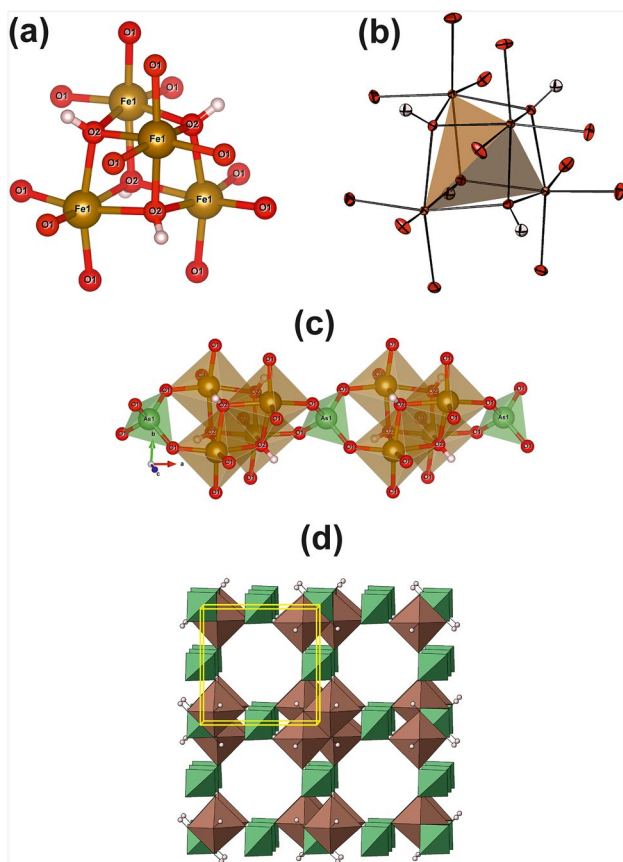**Fig. 3** (**a**) Clusters $Fe_4(OH)_4O_{12}$ of four edge-sharing $FeO_3(OH)_3$-octahedra, bonding *via* hydroxyl anions $O2H2^-$, (**b**) four nearest neighboring Fe(III) cations (displacement ellipsoids are drawn at the 50% probability level) occupy vertices of an regular tetrahedron, centered at the origin of the unit cell in Tpsd, (**c**) clusters (brown) corner-linked to AsO_4-tetrahedra (green), (**d**) heteropolyhedral framework $[Fe_4(OH)_4(AsO_4)_3]^-$ in the zeolite-like crystal structure of Tpsd viewed nearly along [0 0 1]. A trace of the unit cell is drawn for reference

$AsO1_4$-tetrahedra, each sharing two vertices with one $M_4(O2H2)_4O1_{12}$ cluster, are further connected to form a mixed tetrahedral–octahedral open 3D framework $[M_4(O2H2)_4(AsO1_4)_3]^-$ (Fig. 3d). In that way in a 3D framework, each $AsO1_4$-tetrahedron is connected to four M atoms in two adjacent $M_4(O2H2)_4O1_{12}$ clusters (Fig. 3c). The metal centers distance M–M in Tpsd is 3.2161(1) and in Tpal is 3.0562(2) Å, whereas the As–Fe distance is 3.2682(1) and the As–Al is 3.1754(2) Å.

The 12 oxygen atoms O1 serve as bridges between clusters and are shared with the surrounding arsenate groups. The As–O1 bonds in arsenate tetrahedra of 1.687(4) and 1.683(4) Å in Tpsd and Tpal, respectively, are slightly shorter than the sum of the effective ionic radii reported by Shannon (1976) for As(V) in tetrahedral coordination and O^{2-} (0.335 + 1.38 = 1.715 Å), but equal to the average bond lengths of 1.687 Å reported by Gagné and Hawthorne

(2018) (Table 3). Their bond valence sums are $\Sigma\nu_i = 4.96$ v.u. and $\Sigma\nu_i = 5.02$ v.u. in Tpsd and Tpal, respectively, which is almost identical to the formal charges of the tetrahedrally coordinated As(V) cations. Considering contributions from only M(III) and As(V) cations, the bond valence sum for O1 is $\Sigma\nu_i = 1.859$ v.u. in Tpsd and $\Sigma\nu_i = 1.864$ v.u. in Tpal. Including some small contribution from the Tl-atom, the bond valence sum reaches a value close to the oxygen charge of –2. Taking into account contributions from three M(III) atoms and if the contribution of hydrogen is 0.8 v.u., the bond valence sum around O2 atom is $\Sigma\nu_i = 2.06$ v.u. in Tpsd and $\Sigma\nu_i = 2.02$ v.u. in Tpal, which is equal to its oxidation state.

The large interpenetrating channels centered at 0½½, host Tl atoms, hydroxyl groups and H_2O molecules. In order to neutralize the –1 charge of the $[M_4(OH)_4(AsO_4)_3]^-$ framework, one positive charge of Tl(I) cation is needed, but the structure refinement and chemical analysis suggest that there is more than one Tl(I) cation per formula unit (pfu) in both structures. In Tpal, Tl1 atom is located exactly at the center of the unit-cell face (3c special position at 0½½, site occupation factor is 0.417) and has the large anisotropic displacement ellipsoid elongated along the Tl1–O4 bonds (Fig. 4b). In Tpsd, the Tl1a atoms are situated at the center (Tl1a atoms occupy one-sixth of the 3c special position), but Tl1b are slightly displaced from the ideal position at 0½½ and are distributed near the center (Tl1b atoms occupy one-third of the 6 g special position x ½ ½, $x = 0.0578(3)$) of the (001) face. In the other words, besides not fully occupied special 3c (Tl1a) site (center of the (001) face), Tpsd contains one additional 6 g (Tl1b) site, which is split in two symmetrically equivalent positions close to the Tl1a [Tl1a–Tl1b = 0.461(3) Å], with less than half-occupancy each (Fig. 4c, d, Tables 2 and 3). The structure refinement of the site occupancy factors, using separate positional and atomic displacement parameters, confirms that in Tpsd atoms Tl1a occupy 0.5 of the 3c and Tl1b occupy 2 of the 6 g available sites, respectively. In Tpal, Tl1 occupies 1.25 of the 3c positions (41.67% of available sites). During the last refinement cycles, the site occupancies of Tl atoms were fixed. No close Tl–Tl distances were observed in Tpsd or in Tpal.

The most probable way in which cation–anion balance in Tpsd and Tpal compounds may be maintained, is to locate 1.5 OH^- groups in Tpsd and 0.25 OH^- groups in Tpal. The oxygen O5 from the hydroxyl group, whose presence is required to maintain charge neutrality, were found in the center of the unit cell at ½½½, the special 1b site and according to the refinement of the occupation parameters, O5 is half-occupied in Tpsd and quarter-occupied in Tpal, indicating that each 4e site host oxygen O4 of three H_2O molecules and one hydroxyl group in Tpsd, but in Tpal is fully occupied by H_2O molecules.
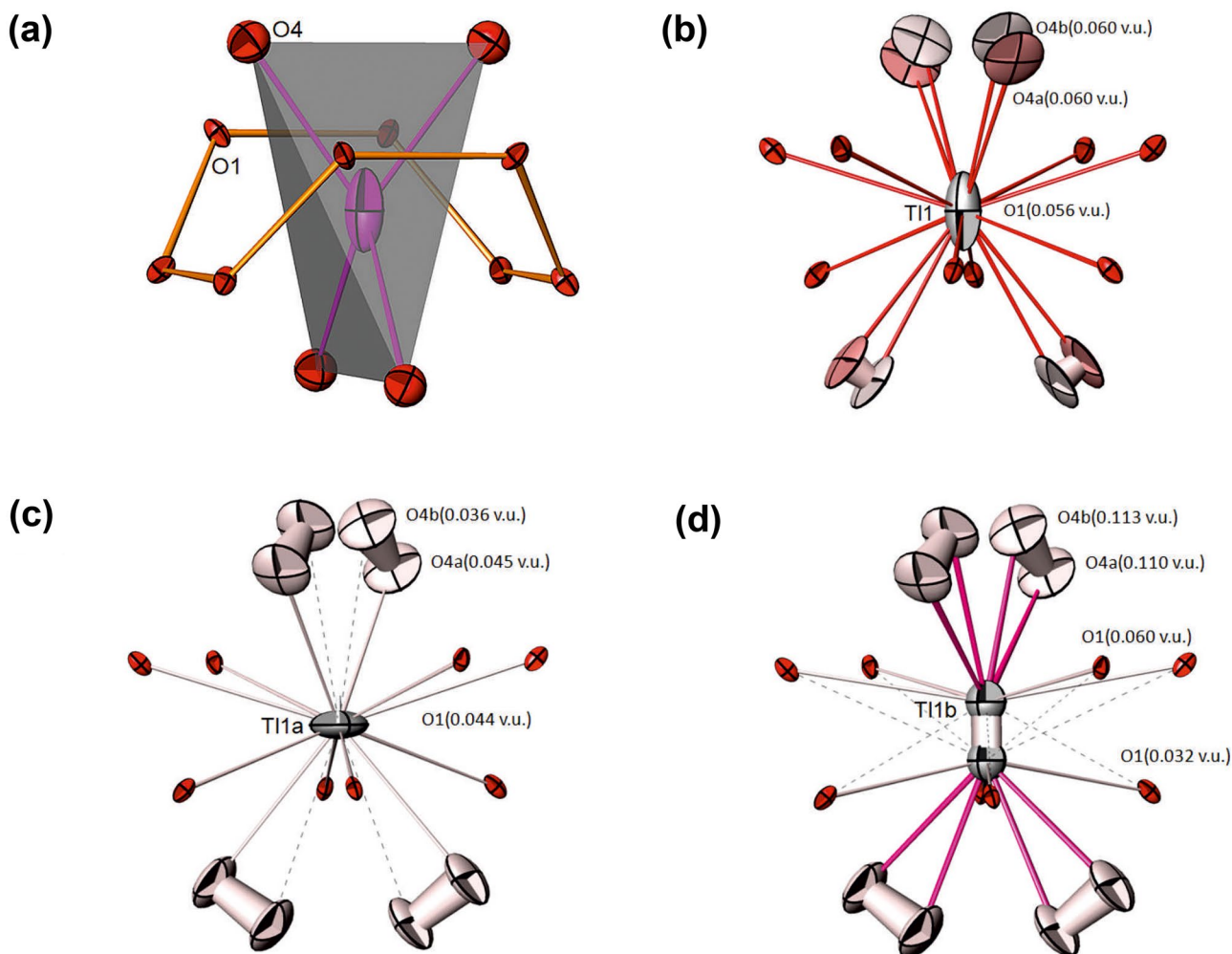
Fig. 4 (**a**) The coordination environment of Tl atom in pharmacosiderite structure-type viewed along the $[\bar{1}\ 0\ 3]$ axis. Undistorted O4 atoms build a sphenohedral polyhedron (grey) around the Tl atom. With the addition of the eight closest O1 atoms (eight-membered ring in the central part of the coordination polyhedron), a cuboctahedral surrounding is completed, (**b**) the environment around the Tl1 in Tpal, (**c**) the environment around Tl1a and (**d**) Tl1b in Tpsd, formed by oxygen atoms O4a and O4b in split positions with high anisotropic displacement parameters (displacement ellipsoids are drawn at the 50% probability level) and by eight oxygen atoms O1. Parameters [Ro; B] for calculation of the bond valences were taken from http://www.iucr.org/resources/data/datasets/bond-valence-parameters

Neglecting the positional disorder of four symmetry equivalent O4 atoms, they would form an undistorted sphenohedral environment around the Tl atom in the center of the (001) face (Fig. 4a). With additional eight O1 oxygen atoms, which are bonded to the central atom Tl at Tl–O distances of similar lengths (Table 3), they complete the coordination polyhedron with CN = 4 + 8. Despite of the positional disorder of O4 atom, similar coordination polyhedron with CN = 4 + 8 was found in Tpal (Fig. 4b) with comparable bond lengths Tl1–O4a of 3.168(2) or Tl1–O4b of 3.166(5) and Tl1–O1 of 3.192(2) Å. However, the size and the elongation of the anisotropic displacement ellipsoids of the Tl1, O4a and O4b atoms indicate the presence of disorder in both structures (Fig. 4). The corresponding average bond lengths (Table 3) of 3.184 Å (or 3.183 Å), are slightly shorter than the <Tl(I)–O> reported average of 3.195 Å (Gagné and Hawthorne 2018), but still within the general range of Tl(I)–O bond distances in the Tl(I)-coordination polyhedron with CN = 12.

In the structure of Tpsd, Tl atoms are located at two very close and not fully occupied sites: Tl1a at 3c and Tl1b at 6g position at Tl1a–Tl1b splitting distance of 0.461(3) Å (Table 3). Similar to the Tl1 atoms in Tpal structure, each Tl1a atom in Tpsd is coordinated by eight oxygen atoms O1 at Tl1a–O1 distances of 3.2761(17) Å and four statistically distributed O4a atoms at similar distances (Tl1a–O4a = 3.271(2) Å) or another four statistically distributed O4b atoms at longer Tl1a–O4b distances of 3.358(6) Å (Fig. 4c, Table 3). All distances are still within the general range from 4.012 to 2.722 Å for Tl(I)–O bond distances and coordination number 12 (Gagné and Hawthorne 2018).

Splitting over two symmetrically equivalent positions, Tl1b is slightly displaced from the center of the (100) face toward the center of the unit cell. In that way it approached the O5 atom at the distance of 3.522(2) Å. This Tl1b–O5 bond distance in Tpsd is the shortest distance between O5 and Tl atoms in Tpsd and Tpal. The other distances (Tl1a–O5 = 3.9823(1) and Tl1b–O5 = 3.8640(2) Å in Tpsd and Tpal, respectively) are considerably longer (Table 3). Every Tl1b atom is also coordinated by four statistically distributed O4-atoms, one half of which is at shorter (Tl1b–O4a = 2.942(4) and Tl1b–O4b = 2.932(5) Å) and the other at much longer distances (Tl1b–O4a = 3.629(2) and Tl1b–O4b = 3.792(8) Å). Besides, four oxygen O1 atoms are at shorter (Tl1b–O1 = 3.166(2) Å) and additional four O1 are at longer Tl1b–O1 distances of 3.445(2) Å (Fig. 4, Table 3).

The O4 position in Tpsd is split into 56(2)% occupied O4a site and 44(2)% occupied O4b site, while the O4 position in Tpal is split into 72(4)% occupied O4a site and 28(4)% occupied O4b site. The splitting O4a–O4b distances are 1.19(3) and 0.57(5) Å for Tpsd and Tpal, respectively (Table 3). The site occupation factors of O4a and O4b atoms were refined using separate positional and the same atomic displacement parameters. To attain charge neutrality in Tpsd, three O4 atoms are from H_2O molecules, and one is from the hydroxyl group. These models give the fully balanced formulae $Tl_{2.5}Fe_4[(AsO_4)_3(OH)_4](OH)_{1.5} \cdot 3H_2O$ for Tpsd and $Tl_{1.25}Al_4[(AsO_4)_3(OH)_4](OH)_{0.25} \cdot 4H_2O$ for Tpal.

The O2 oxygen atoms of hydroxyl group $O2H2^-$ are hydrogen-bonded to the O4a oxygen atoms by medium–strong linear hydrogen bonds whose O⋯O lengths are O2⋯O4a = 2.648(19) in Tpsd and O2⋯O4a = 2.65(2) Å in Tpal. Four symmetry equivalent 4e positions, which are alternatively and partially occupied by H5 atoms, form around oxygen O5 an ideal tetrahedron dictated by the symmetry. This statistically distributed hydroxyl group $O5H5^-$ is bonded also linearly to the O4a by hydrogen bonding interactions whose O⋯O length are similar, i.e. O5⋯O4a = 2.655(18) in Tpsd, while O5⋯O4a = 2.52(2) Å in Tpal.

Crystal chemistry and structural properties of Tl_3AsO_4

As already mentioned, the crystal structure of the Tl_3AsO_4 has been determined before (Effenberger 1998). It is hexagonal, space group $P6_3$, with $a = 8.5259(12)$ and $c = 5.238(1)$ Å. It contains six symmetry-equivalent monovalent cations Tl(I) in the unit cell, which are bound by tetrahedral arsenate anions. In the Tpsd and Tpal structures, Tl(I) cations are located in the center of the channels with their lone-electron pairs filling channels, while in the Tl_3AsO_4 structure, Tl is positioned on the walls of the channels (Fig. 5a). The cation Tl(I) is strongly lone-pair stereoactive with three short Tl–O bonds to one side of the Tl(I) cation. With three nearest O atoms [Tl–O bonds 2.532(8), 2.547(4), 2.570(9) Å], Tl(I) cations make characteristic trigonal pyramids with a cation at the apex and corresponding angles not deviating much from 90° (Table 3, Fig. 5b). If two additional bonds at 3.324(9) and 3.508(8) Å are accounted for, these Tl atoms are in quite deformed coordination geometry intermediate between square pyramidal and trigonal bipyramidal. Both average bond lengths of < 2.550 > for CN = 3 and < 2.896 > for CN = 5 (Table 3) are slightly longer than the reported average of 2.517 and 2.840 Å, respectively (Gagné and Hawthorne 2018). The next seven O atoms are at very long distances ranging from 3.628(9) to 4.942(8) Å. It is interesting that all bonds are situated to the one side of the Tl(I) cation. With increasing coordination number, the asymmetric distribution of coordinating anions is not lost. Considering only the contributions of the nearest three O atoms, bond valence calculations indicated a small charge deficiency for Tl(I) cation i.e. $\Sigma\nu_i = 0.95$ v.u. However, when we take into account the contributions of the next two O atoms at longer distances, the bond valence for Tl(I) is well balanced, i.e. $\Sigma\nu_i = 1.01$ v.u. for CN = 5. The contributions of seven additional long bonds are very small and equal to 0.047 v.u. for all of them.

The length of three As–O2 bonds in AsO_4-tetrahedra is 1.681(7) Å (1.262 v.u.). The fourth As–O1 bond of 1.731(13)

Fig. 5 (**a**) The projection of the crystal structure of Tl_3AsO_4 approximately along [001] with channels hosting lone electron pairs of Tl(I) cations (dark grey spheres). The TlO_5 polyhedra (light grey) are bonded by AsO_4 tetrahedra (green); (**b**) The five nearest neighboring oxygen atoms (displacement ellipsoids are drawn at the 50% probability level) in the coordination polyhedron (CN = 3 + 1 + 1) distorted by the lone-electron-pair activity of Tl(I) cations viewed along the [1 4̄ 3] axis

(a)

(b)

O2(0.024 v.u.)

Tl1

O2(0.039 v.u.)

O1(0.319 v.u.)   O2(0.300 v.u.)   O2(0.332 v.u.)
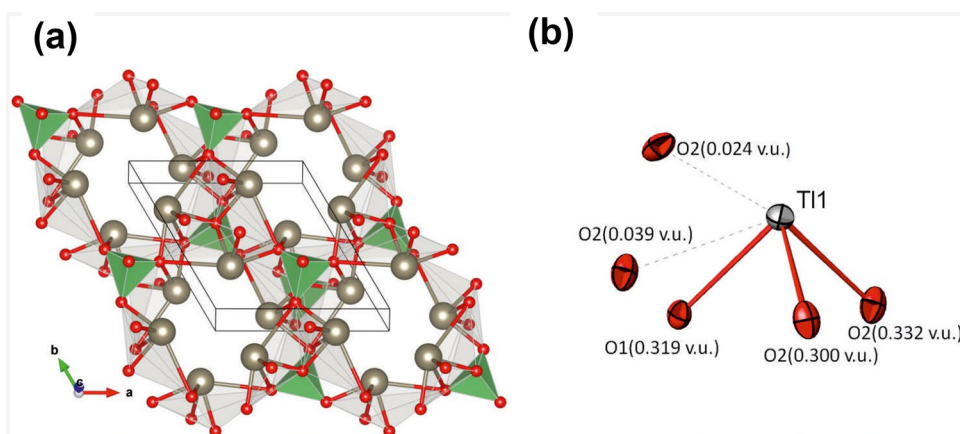
Å (1.102 v.u.) is slightly longer and the bond valence sum for the As1 atom is $\Sigma\nu_i = 4.89$ v.u. for CN = 4, which is nearly equal to its oxidation state. Actually, O1 atom is also involved in three short Tl1–O1 bonds of 2.547(4) Å, so the bond valence sum for O1 is $\Sigma\nu_i = 2.06$ v.u. for CN = 4. The sum of the bond valences around O2 atom is $\Sigma\nu_i = 1.96$ v.u. for CN = 5 (one As1 and 4 Tl1), which is almost equal to its oxidation state. A slightly longer average < As—O > bond lengths of 1.694 Å than the reported average of 1.687 Å (Gagné and Hawthorne 2018) and a BVS of 4.89 v.u. of the As atom, shows a quite usual slightly deformed AsO_4-group in the Tl_3AsO_4 structure.

The shortest Tl–Tl distance is 3.7778(5) Å, which is close to the sum of the van der Waals radii of 3.92 Å (Bondi 1964), suggest the absence of significant interactions between Tl-neighbors. The tendency of Tl(I) ions to make Tl–metal contacts, that are (sometimes much) shorter than the sum of corresponding van der Waals radii, is well known. Among them, the Tl–Tl contacts, which are shorter than 3.92 Å, have been found in many classes of the compounds (Karanović et al. 2008). The residual electron density map is low except the small symmetry-equivalent peaks around 00½ and 000 (2a site) 2.72 Å away from the Tl1 site, indicating that very small amount of H_2O molecules is probably entering the channel.

Raman spectra of Tpsd, Tpal and Tl_3AsO_4

Pharamcosiderite-group arsenates are common minerals in near-neutral As-rich soils and mining wastes, where they mostly appear in the form of nano-sized cubes or as poorly-crystalline aggregates (Majzlan et al. 2014; Drahota et al. 2018; Morin et al. 2002).Therefore, it is of exceptional importance to be familiar with their Raman spectra, since in the combination with electron microscopy based chemical analyses it is sometimes the only possible analytical method for their identification. In our previous work on mineralogy of mining wastes and technosols from the Tl-, Fe- and As-extremely rich locality Crven Dol (Allchar deposit, North Macedonia), we have recorded Raman spectrum of poorly crystallized thalliumpharmacosiderite intergrown with dorallcharite (Đorđević et al. 2021a) (959, 876, 788, 475, 390, 243, and 192 cm^{-1}). Compared to the spectrum of natural pharmacosiderite (Đorđević et al. 2021a) (Fig. 6a), the spectrum of Tpsd (Fig. 6b) shows small differences in band intensities and positions, but overall is quite similar to its natural analogue (Fig. 6a) and with structurally related pharmacosiderite-type arsenates (Frost and Kloprogge 2003; Filippi et al. 2007). Thus, the assignments of the absorption bands could be made as follow: in Tpsd a strong band around 866 cm^{-1} could be assigned to the ν_3, and the band at 814 cm^{-1} assigned to ν_1 vibrational modes. The band at 784 cm^{-1} may be assigned to the OH deformation mode.

Raman spectrum of Tpsd exhibits the strongest band at 474 cm^{-1} assigned to the bending ν_4 mode. The ν_2 bending mode of Tpsd is observed at 383/302 and 305/380 cm^{-1}. The bands centered at 190/189, 235/237 cm^{-1} may be assigned to the Fe–O stretching vibrations. The natural and synthetic thalliumpharmacosiderites have different contents of Tl. Thus, their Raman spectra differ especially in the intensities of the ν_1 and ν_3 modes, and in spectral features between 100 and 300 cm^{-1} the shifts are not distinctive. Raman spectra of the synthetic Tpal (Fig. 6c) (151, 318, 383, 589, 650, 838, 915 cm^{-1}) could be compared with natural pharmacoalumite (320, 383, 590, 623, 649, 856, 913 cm^{-1}) from the rruff.info database (RRUFF Number: R060411) (Fig. 6d). Unfortunately, there are no other published Raman spectra of the pharmacoalumite–group minerals.
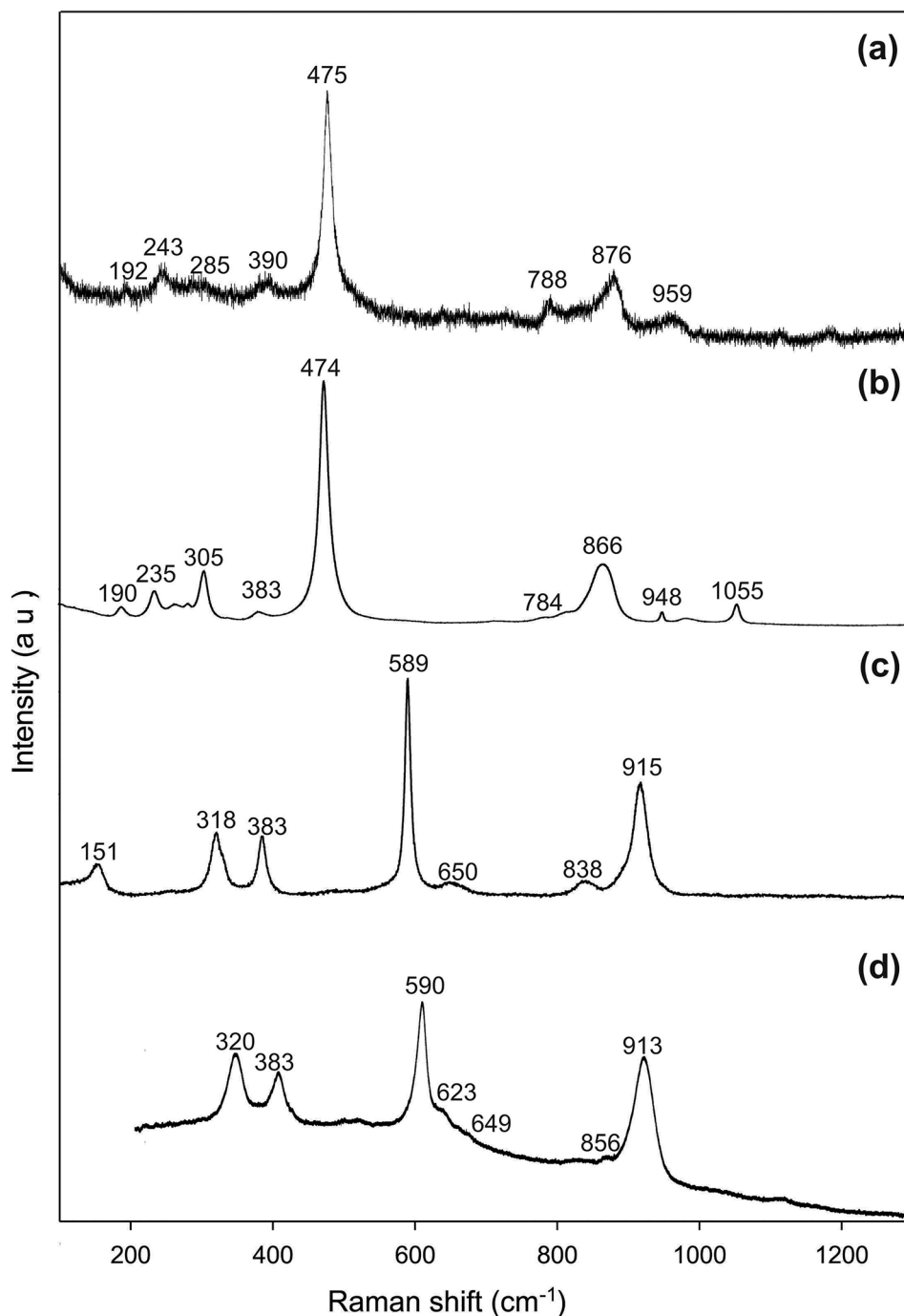
Raman spectra of $TlAsO_3$ (Fig. 1S) and new Tl-Fe-arsenate (Fig. 2S) with their characteristic Raman shifts are presented in the supplementary file. The depiction of their Raman spectra is of very important, since they could be found in naturally Tl- and As-rich environments. Besides the combination of electron microscopy based chemical analyses, the Raman spectra could be the most promising analytical method for their characterization.

Transmission electron microscopy of Tpsd

In order to confirm the structure of Tpsd and the oxidation sate of iron FIB lamellae were analysed in TEM by means of EELS, EDS and SAED. TEM-micrograph (Fig. 7) showed that the beam damage occurs immediately, thus causing dark areas containing more Tl. The reason is that OH-groups and the crystallisation water leave the specimen. A slight re-ordering of the residual atoms in the bright areas was observed. Selected area diffraction (SAED) patterns (Fig. 8) gave slightly larger unit-cell than measured by SC-XRD ($a = 8.07$ Å, Fig. 8). The observed discrepancy is most probably due to the discrepancy in chemical composition measured by TEM-EDS and that obtained through SC-XRD.

TEM–EELS was applied to quantify the oxidation states of Fe in Tpsd as a function of the integral ratio of Fe L_3/L_2 ionization edge (van Aken and Liebscher 2002) (Fig. 8). For this purpose, the area of a 2 eV energy window below the L_3 and L_2 white lines is determined after the subtraction of the continuum states fitted by a double arctan-function. Details are described by van Aken and Liebscher (2002). In the present sample the L_3/L_2 ratio is 5.1, thus indicating that Fe is in its Fe(III)-state. A similar check of the oxidation state could be done at the Tl-L edge (see for example Wick et al. 2018, 2019, 2020). However, due to the fact that the Tl-L edge is at energy losses of more than 12.68 keV, it is only accessible with X-ray absorption spectroscopy, but not with EELS. The only Tl-edge being accessible with EELS is the Tl-M edge at 2389 eV energy

Fig. 6 Raman spectra of (**a**) thalliumpharmacosiderite, $TlFe_4(AsO_4)_3(OH)_4 \cdot 4H_2O$, from Crven Dol locality, Allchar deposit, (**b**) synthetic Tpsd, $Tl_{2.5}Fe_4[(AsO_4)_3(OH)_4](OH)_{1.5} \cdot 3H_2O$ (**c**) synthetic Tpal, $Tl_{1.25}Al_4[(AsO_4)_3(OH)_4](OH)_{0.25} \cdot 4H_2O$ and (**d**) pharmacoalumite from the RRUFF database (Number: R060411)

Thalliumphrmacosiderite in nature

Pharmacosiderite-group minerals occur at many sites, but usually in small amounts and often as a minor, inconspicuous phase. At some localities, pharmacosiderite may be an important or the dominant carrier of As (Drahota et al. 2009,

loss, which is not sensitive to the valence state. Thus, the valence state of Tl was not determined.

2018; Herrmann et al. 2018). Those occurrences seem to be connected to slow weathering under circumneutral conditions. Hence, even at sites where substantial acidity is developed, pharmacosiderite could crystallize in microenvironments that are able to neutralize that acidity.

Thalliumpharmacosiderite is not an abundant mineral, but in As and Tl harsh environments, it could be an important Tl and As sink. According to the known literature data and the Mindat Home Page, it has been reported to exist in mining

Fig. 7 Bright-field TEM micrograph of Tpsd, $Tl_{2.5}Fe_4[(AsO_4)_3(OH)_4]$ $(OH)_{1.5} \cdot 3H_2O$ showing the dark areas with more Tl due to the beam damage

crust-like aggregates and it is intergrown with dorallcharite, $TlFe^{3+}_3(SO_4)_2(OH)_6$. (Fig. 3S). Minor amounts of Tl (up to 1 at%) were also found in pharmacosiderite. There, Tl was found in the locally acidic environments, where it has only been rarely detected in dispersed fine-grained secondary Fe-oxyhydroxides (FOH) and only in amounts below 0.1 wt%, close to the detection limit. On the contrary, in the neutral to slight alkaline environments of the Crven Dol locality, no occurrence of thalliumpharmacosiderites has been detected. In these environments we observed the predominance of Ca(II)-Fe(III)-arsenates (arseniosiderite) and Tl is retained in the novel, poorly-crystalline Tl-arsenates (Đorđević et al. 2021a). Yet, Tpsd was found in the carbonate-buffered tailings at another locality of Allchar-deposit near Adit 25 (Đorđević et al. 2021c) in the paragenesis with Ca-Fe- and Ca-Mg-arsenates, which confirm its stability over the wider pH-range. From the Oleninsky ore occurrence in Russia (Kalinin and Savchenko 2019), the existence of a phase similar in composition to thalliumpharmacosiderite was just briefly mentioned and no data on its chemical composition, nor detailed description of its occurrence was reported. Thalliumpharmacosiderite probably forms through aging, remobilization and recrystallization of As-rich hydrous ferric oxide (HFO) in Tl-harsh environments under near neutral conditions, under which arsenian HFO is less soluble than scorodite, $FeAsO_4 \cdot 2H_2O$ (Haffert et al. 2010).

At all studied sites, quantitative mineralogical analyses have shown that the proportion of As hosted by the pharmacosiderite-group minerals decreases systematically from the saprolite to the topsoil; in the upper soil horizons, the system evolves toward As-rich Fe oxides, probably *via* solid-state reaction (Morin et al. 2002; Drahota et al. 2018; Bossy

ore deposits and mining wastes at only two localities worldwide: Allchar deposit, North Macedonia (Đorđević et al. 2021a) and Oleninsky ore occurrence at Vorontsovskoe gold deposit in Northern Urals, Russia (Kalinin and Savchenko 2019). In the mining wastes and technosols at the "Crven Dol" locality of Allchar deposit, thalliumpharmacosiderite was characterized by EMPA, SEM–EDS, and Raman spectroscopy (Đorđević et al. 2021a). It appears in the form of tiny cubic crystals (~2 μm) or as poorly crystalline,

Fig. 8 (**a**) TEM-SAED of the Tpsd, $Tl_{2.5}Fe_4[(AsO_4)_3(OH)_4](OH)_{1.5} \cdot 3H_2O$ and (**b**) Fe-ELNES for the determination of the valence state of Fe in Tpsd

et al. 2010). These observations imply that pharmacosiderite forms in deep saprolite where constantly high dissolved As and Fe concentrations are maintained owing to slow groundwater flow. The increasing Fe/As molar ratio and/or decreasing Fe and As concentrations during pedogenesis destabilizes pharmacosiderite and drives its transformation into As-rich Fe oxides.

Our research has been intended to improve the understanding of formation conditions, crystal structure and the chemical compositions of the compounds in the Tl(I)–M(III)–As(V)–H_2O (M = Al, Fe) system, especially members of the pharmacosiderite- and pharmacoalumite-group of minerals. As confirmed with the new chemical formula of the synthetic Tpsd, the more trivial problem is the variable H_2O content, which is not surprising for a zeolite-like phase. However, a number of studies reported a substantial excess of exchangeable cations, such as K, Na, or Ba, in pharmacosiderite (Table 4). Bariopharmacosiderite may contain up to 1.0 Ba atom pfu. The possibility of charge balance *via* reduction of Fe(III) to Fe(II) was excluded by Mössbauer spectroscopy. Another, more viable, possibility is the removal of H^+ ions from the structure, either by deprotonation of a H_2O molecule or dehydroxylation of a bridging OH^- group.

Environmental implications

Together with sulfate minerals, arsenate minerals play a pivotal role in the sequestration and transport of potentially toxic and bioavailable metals and metalloids released through weathering of ore deposits, abandoned mines and the surrounding mining wastes, as well as through coal combustion, ferrous and non-ferrous mining/smelting activities and cement production (Vaněk et al. 2011, 2018, 2021, 2022 and references therein). Consequently, the characterization of the mineralogy and geochemistry of their oxidation products is vital for predicting of their environmental impact and the solid-phase controls on dissolved metal concentration (Jamieson 2011; Lottermoser 2010, 2017). This characterization involves the precise knowledge of the crystal chemistry of arsenate minerals, a goal that can be achieved only through a multi-technique approach, including chemical, structural, and spectroscopic data.

As a lithophile element, Tl^+ tends to substitute for K^+ in minerals such as K-feldspars, micas and micaceous clay minerals due to their similar ionic radii. Thus, one of its natural sources is the weathering of K-rich rocks (Vaněk et al. 2009). As a chalchophile element, Tl occurs as a trace constituent in pyrite and other sulfides (marcasite, galena, sphalerite, stibnite, realgar) and sulfosalts (geocronite, boulangerite, jordanite). Quite a few minerals contain Tl as their main constituent, mostly primary sulfosalts (i.e., lorándite, bernardite, fangite). Accordingly, its second natural source arise through weathering of metal-sulfide deposits and mining activities connected to them (Aguilar-Carrillo et al. 2018; Cruz-Hernández et al. 2018; Garrido et al. 2020; Gomez-Gonzalez et al. 2015). Exceptionally, Tl may also become significantly concentrated in Tl-deposits, as demonstrated by

Table 4 The arsenates with the pharmacosiderite and pharmacoalumite group minerals with different exchangeable cations

Mineral name	Chemical formula	a (Å)	c (Å)	V (Å³)	Reference
Pharmacosiderite group					
Bariopharmacosiderite-Q	$Ba_{0.5}Fe^{3+}_4(AsO_4)_3(OH)_4 \cdot 6.16H_2O$	7.947(1)	8.049(2)	508.3(1)	Hager et al. (2010)
Bariopharmacosiderite-C	$Ba_{0.5}Fe^{3+}_4(AsO_4)_3(OH)_4 \cdot 2.52H_2O$	7.942(1)	–	500.9(1)	Hager et al. (2010)
Strontiumpharmacosiderite*	$Sr_{0.5}Fe_4[(AsO_4)_3(OH)_4] \cdot 4H_2O$	8.084(27)	8.151(5)	532.676	Mills et al. (2014)
Caesiumpharmacosiderite*	$CsFe_4(AsO_4)_3(OH)_4 \cdot 4H_2O$	7.9637(11)	–	505.062	Mills et al. (2013)
Hydroniumpharmacosiderite	$(H_3O)Fe_4(AsO_4)_3(OH)_4 \cdot 4H_2O$	7.9587(2)	–	504.11(2)	Mills et al. (2010a, b)
Natropharmacosiderite	$Na_2Fe^{3+}_4(AsO_4)_3(OH)_5 \cdot \sim 7H_2O$	7.928(9)	–	498.3(9)	Hager et al. (2010)
Pharmacosiderite*	$KFe^{3+}_4(AsO_4)_3(OH)_4 \cdot 6\text{-}7H_2O$	7.9816(1)	–	508.48	Buerger et al. (1967)
Plumbopharmacosiderite	$Pb_{0.5}Fe^{3+}_4(AsO_4)_3(OH)_4 \cdot 5H_2O$	7.9791(2)	–	508.00(6)	Vignola et al. (2018)
Thalliumpharmacosiderite*	$TlFe_4(AsO_4)_3(OH)_4 \cdot 4H_2O$	7.9878(1)	–	509.51	Rumsey et al., (2014)
"Thalliumpharmacosiderite" (synthetic)	$Tl_{2.5}Fe_4[(AsO_4)_3(OH)_4](OH)_{1.5} \cdot 3H_2O$	7.9645(1)	–	505.21(2)	This work Tpsd
Pharmacoalumite group					
Bariopharmacoalumite	$Ba_{0.5}Al_4(AsO_4)_3(OH)_4 \cdot 5H_2O$	7.742(4)	–	464.2(4)	Mills et al. (2011)
Hydroniumpharmacoalumite	$(H_3O)Al_4(AsO_4)_3(OH)_4 \cdot 4.5H_2O$	7.7296(2)	–	461.33(4)	Hochleitner et al. (2013, 2015)
Natropharmacoalumite	$Na_2Al_4(AsO_4)_3(OH)_5 \cdot 4H_2O$	7.7280(3)	–	461.53(3)	Rumsey et al. (2010)
Pharmacoalumite	$KAl_4(AsO_4)_3(OH)_4 \cdot 6.5H_2O$	7.745(1)	–	464.584	Schmetzer et al. (1981)
"Thalliumpharmacoalumite" (synthetic)	$Tl_{1.25}Al_4[(AsO_4)_3(OH)_4](OH)_{0.25} \cdot 4H_2O$	7.7281(4)	–	461.55(7)	This work Tpal

the large amounts of Tl occurring in some sulfide mineral deposits, i.e. Xiangquan, China, the world's solitary Tl-only mine, which hosts around 250 tons of Tl (Zhou et al. 2005), Allchar deposit, North Macedonia, which hosts approximately 500 tons of Tl (Janković and Jelenković 1994) and Meggen deposit, Germany that contains 960 tons of Tl, the largest accumulation on Earth (Laznicka 2010).

The natural weathering of Tl-bearing sulfide minerals may sometimes induce lower Tl release rates to the environment, which may have an effect on the types of secondary Tl-bearing minerals and sorption processes that ultimately control Tl bioavailability (Garrido et al. 2020 and references therein). In natural multi-component systems, only few phases have been identified to control Tl solubility. In the environmental media with lower Tl-concentration (e.g. soils), Tl(I) adsorption onto micaceous phyllosilicates (mostly illite), followed by Tl(I) and Tl(III) adsorption onto Mn-oxides has previously been identified as the dominant Tl retention mechanism. However, in Tl-extreme environments, when phyllosilicates (micas), illite-type clays and Mn-oxides are either absent or exhausted, secondary Tl minerals (mainly arsenates and sulfates) form and store Tl (Đorđević et al. 2021a).

There are only several naturally occurring secondary Tl minerals whose crystal chemistry has been described. Chemically, they are mainly Tl-oxides and Tl-oxysalts, such as arsenates and sulfates. They are usually tiny and/or poorly-crystalline, thus often unsuitable for conventional structure analysis using single-crystal X-ray diffraction. Among others, we can mention the minerals dorallcharite, $TlFe^{3+}_3(SO_4)_2(OH)_6$ (Balić-Žunić et al. 1994), lanmuchangite, $Tl^+Al(SO_4)_2 \cdot 12H_2O$ (Chen et al 2001), thalliumpharmacosiderite, $TlFe_4[(AsO_4)_3(OH)_4] \cdot 4H_2O$ (Rumsey et al. 2014), whose crystal structure is still pending, thalliomelane, $Tl(Mn^{4+}_{7.5}Cu^{2+}_{0.5})O_{16}$ (Gołębiowska et al. 2021) and avicennite, Tl_2O_3 (Karpova et al. 1958). In addition, there is a whole suite of Tl-arsenates (Đorđević et al. 2021a; Steinfeld et al. 2021) and Tl-Sb-oxides (Đorđević et al. 2021b) from the well-known Allchar deposit in North Macedonia, whose structure and precise chemical composition remain undetermined. All of them are tightly connected with oxidative weathering of Tl-containing sulfosalts.

Thalliumpharmacosiderite, similarly to the other pharmacosiderite-group arsenates, crystallize in the late stages of weathering of Fe- and As- rich materials, such as ores, solid mining wastes and the surrounding technosols (Herrmann et al. 2018; Majzlan et al. 2019), covering the broad pH stability range (from the acidic to the circumneutral environments), as also suggested by our synthetic experiments. Furthermore, this behavior implies that Tl can be slowly sequestered by Tl-arsenates during the late stages of weathering and thus be permanently retained in thalliumpharmacosiderite and/or in Tl-bearing pharmacosiderites.

Conclusions

The low crystallinity of Tl and As containing minerals in the systems Tl(I)–M(III)–As(V)–H_2O (M = Al, Fe) and Tl(I)–As(V)–H_2O has made a detailed understanding of their crystal structures hard to define. To avoid the problem of low crystallinity and gain more details on the crystal structures, the synthesis of single crystals was undertaken. Single-crystals of Tpsd and Tpal were synthesized in relatively broad pH range (pH = 3–7). Therefore, they play an important role in the sequestration of Tl in circumneutral systems, but also in acid mine drainage systems, where they can crystallize in the micro-environments. Tpsd probably forms upon aging, remobilization and recrystallization of As-rich ferrihydrite in Tl- and As-rich environments under near neutral conditions, when arsenical ferrihydrite is less soluble than scorodite. Tpsd is reported to exist at only two different localities worldwide (Allchar mine, North Macedonia and Olenienskoe gold deposit, Murmansk Oblast, Russia). Tpal was not reported as a mineral, but could be potentially found in nature.

SC-XRD-analyses of Tpsd and Tpal provide a more complete understanding of their crystal structures. Both FeO_6 and AlO_6 octahedra have $3 + 3$ coordination, while As is found at the tetrahedral site. The structure refinement of the occupation parameters confirms that in Tpsd Tl atom Tl1a occupies 0.5 of the 3c and Tl1b occupies 2 of the available 6 g sites. The oxygen O5 from the hydroxyl group, whose presence is required to maintain charge neutrality, was found in the center of the unit cell at the special 1b site and according to the refinement of the occupation parameters, it is half-occupied in Tpsd and quarter-occupied in Tpal. Consequently, each 4e site, which host disordered oxygen O4, in Tpal is fully occupied by H_2O molecules, but in Tpsd is occupied by three H_2O molecules and one hydroxyl group. The channels in Tl_3AsO_4 structure mainly contain lone electron pairs of Tl atoms, which are five-coordinated and has very asymmetric coordination with two longer and three shorter Tl–O bonds.

References

Aguilar-Carrillo J, Herrera L, Gutierrez EJ, Reyes-Domínguez IA (2018) Solid-phase distribution and mobility of thallium in mining-metallurgical residues: environmental hazard implications. Environ Poll 243:1833–1845

Aguilar-Carrillo J, Herrera-García L, Reyes-Domínguez IA, Gutiérrez EJ (2020) Thallium(I) sequestration by jarosite and birnessite: structural incorporation vs surface adsorption. Environ Poll 257:113492–113503

Balić-Žunić T, Moëlo Y, Lončar Z, Micheelsen H (1994) Dorallcharite, $Tl_{0.8}K_{0.2}Fe_3(SO_4)_2(OH)_6$, a new member of the jarosite-alunite family. Eur J Mineral 6:255–263

Biagioni C, D'Orazio M, Lepore GO, d'Acapito VS (2017) Thallium-rich rust scales in drinkable water distribution systems: A case study from northern Tuscany, Italy. Sci Total Environ 587:491–501

Bondi A (1964) Van der Waals Volumes and Radii. J Phys Chem 68:441–451

Bossy A, Grosbois C, Beauchemin S, Courtin-Nomade A, Hendershot W, Bril H (2010) Alteration of As-bearing phases in a small watershed located on a high-grade arsenic-geochemical anomaly (French Massif Central). Appl Geochem 25:1889–1901

Bruker (2007) Bruker SAINT-Plus. Bruker AXS Inc, Madison

Buerger M, Dollase W, Garaycochea-Wittke I (1967) The structure and composition of the mineral pharmacosiderite. Z Kristallogr N Cryst Struct 125:92–108

Chen D, Wang G, Zou Z, Chen Y (2001) A new mineral - Lanmuchangite. Acta Mineral Sinica 21:271–277

Cruz-Hernández Y, Ruiz-García M, Villalobos M, Martin Romero F, Meza-Figueroa D, Garrido F, Hernández-Alvarez E, Pi-Puig T (2018) Fractionation and mobility of thallium in areas impacted by mining-metallurgical activities: Identification of a water-soluble Tl(I) fraction. Environ Poll 237:154–165

D'Orazio M, Biagioni C, Dini A, Vezzoni S (2017) Thallium-rich pyrite ores from the Apuan Alps, Tuscany, Italy: constraints for their origin and environmental concerns. Mineral Deposita 52:687–707

Đorđević T, Drahota P, Kolitsch U, Majzlan J, Peřestá M, Kiefer S, Stöger-Pollach M, Tepe N, Hofmann T, Mikuš T, Tasev G, Serafimovski T, Boev I, Boev B (2021a) Synergetic Tl and As retention in secondary minerals: An example of extreme arsenic and thallium pollution. Appl Geochem 135:105114–105130

Đorđević T, Kolitsch U, Drahota, P, Majzlan J, Peřestá M, Tasev G, Serafimovski T, Boev I, Boev B (2021b) Tl sequestration in the middle part of the Allchar Sb–As–Tl–Au deposit, North Macedonia. Goldschmidt Abstracts, 2021. https://doi.org/10.7185/gold2021.5196

Đorđević T, Drahota P, Kolitsch U, Majzlan J, Kiefer S, Tepe N, Hofmann T, Serafimovski T, Tasev G, Boev I, Boev B (2021c) Geogenic thallium-extreme environments: In which secondary phases is Tl(I) incorporated? Mitt Österr Mineral Ges 167:84

Dowty E (2000) ATOMS for Windows. Version 5.1. Shape Software, Kingsport, Tennessee, USA

Drahota P, Rohovec J, Fillipi M, Mihaljevič M, Rychlovský P, Červený V, Pertold Z (2009) Mineralogical and geochemical controls of arsenic speciation and mobility under different redox conditions in soil, sediment and water at the Mokrsko-West gold deposit, Czech Republic. Sci Total Environ 407:3372–3384

Drahota P, Kulakowski O, Culka A, Knappová M, Rohovec J, Veselovský F, Racek M (2018) Arsenic mineralogy of near-neutral soils and mining waste at the Smolotely-Líšnice historical gold district, Czech Republic. Appl Geochem 89:243–254

Effenberger H (1998) Structure investigations of Tl(I)-arsenates(V): $Tl_3(AsO_4)$, $Tl_2Cu(I)(AsO_4)$ and $TlCu(II)_2(AsO_4)(AsO_3OH)$. Z Kristallogr Cryst Mater 213:42–46

Farrugia LJ (2012) WinGX and ORTEP for Windows: an update. J Appl Crystallogr 45:849–854

Filippi M, Doušová B, Machovič V (2007) Mineralogical speciation of arsenic in soils above the Mokrsko-west gold deposit, Czech Republic. Geoderma 139:154–170

Flack HD (1983) On enantiomorph polarity estimation. Acta Crystallogr A39:876–881

Frost RL, Kloprogge JT (2003) Raman spectroscopy of some complex arsenate minerals - implications for soil remediation. Spectrochim Acta A59:2797–2804

Gagné OC, Hawthorne FC (2018) Bond-length distributions for ions bonded to oxygen: metalloids and post-transition metals. Acta Crystallogr B 74:63–78

Gagné OC, Hawthorne FC (2020) Bond-length distributions for ions bonded to oxygen: results for the transition metals and quantification of the factors underlying bond-length variation in inorganic solids. IUCrJ 7:581–629

Garrido F, Garcia-Guinea J, Lopez-Arce P, Voegelin A, Göttlicher J, Mangold S, Almendros G (2020) Thallium and co-genetic trace elements in hydrothermal Fe-Mn deposits of Central Spain. Sci Total Environ 717:137162–137177

George LL, Biagioni C, Lepore GO, Lacalamita M, Agros G, Capitani GC, Bonaccorsi E, d'Acapito F (2019) The speciation of thallium in (Tl, Sb, As)-rich pyrite. Ore Geol Rev 107:364–380

Gołębiowska B, Pieczka A, Zubko M, Voegelin A, Göttlicher J, Rzepa G (2021) Thalliomelane, $TlMn_{7.5}^{4+}Cu_{0.5}^{2+}O_{16}$, a new member of the coronadite group from the preglacial oxidation zone at Zalas, southern Poland. Am Mineral 106:2020–2027

Gomez-Gonzalez MA, Garcia-Guinea J, Garrido F, Townsend PD, Marco J-F (2015) Thallium and manganese complexes involved in the luminescence emission of potassium-bearing aluminosilicates. J Lumin 159:197–206

Haffert L, Craw D, Pope J (2010) Climatic and compositional controls on secondary arsenic mineral formation in high-arsenic mine wastes, South Island, New Zealand, New Zealand. J Georg Geol 53:91–101

Hager SL, Leverett P, Williams PA, Mills SJ, Hibbs DE, Raudsepp M, Kampf AR, Birch WD (2010) The single-crystal X-ray structures of bariopharmacosiderite-C, bariopharmacosiderite-Q and natropharmacosiderite. Can Mineral 48:1477–1485

Herrmann J, Voegelin A, Palatinu L, Mangold S, Majzlan J (2018) Secondary Fe-AsTl mineralization in soils near Buus in the Swiss Jura Mountains. Eur J Mineral 30:887–898

Hochleitner R, Fehr KT, Kaliwoda M, Günther A, Schmahl WW, Park S (2013) Hydroniumpharmacoalumite, IMA 2012-050. CNMNC Newsletter No. 16, August 2013, page 2699. Mineral Mag 77:26952709

Hochleitner R, Fehr KT, Kaliwoda M, Günther A, Rewitzer C, Schmahl WW, Park S (2015) Hydroniumpharmacoalumite, $(H_3O)Al_4[(OH)_4(AsO_4)_3]\cdot 4\text{-}5\,H_2O$, a new mineral of the pharmacosiderite supergroup from Rodalquilar, Spain. N Jahrb Mineral Abh 192:169–176

Jamieson HE (2011) Geochemistry and Mineralogy of Solid Mine Waste: Essential Knowledge for Predicting Environmental Impact. Elements 7:381–386

Janković S, Jelenković R (1994) Thallium mineralization in the Allchar Sb–As–Tl–Au Deposit. N Jahrb Mineral Abh 167:283–297

Kalinin AA, Savchenko YE (2019) Thallium mineralization in the Oleninskoe gold prospect, Kolmozero-Voronya belt. Proceed Fersman Sci Sess 16:240–244 (in Russian)

Karanović LJ, Poleti D, Balić-Žunić T, Makovicky E, Gržetić I (2008) Two new examples of very short thallium-transition metal contacts: $Tl_3Ag_3Sb_2S_6$ and $Tl_3Ag_3As_2S_6$. J Alloys Compd 457:66–74

Karpova KN, Kon'kova EA, Larkin ED, Savel'ev VF (1958) Avicennite, a new mineral. Doklady Akademii Nauk Uzbekistan SSR 2:23–26 (in Russian)

Kasatkin AV, Stepanov SYu, Tsyganko MV, Škoda R, Nestola F, Plášil J, Makovicky E, Agakhanov AA, Palamarchuk RS (2022) Mineralogy of the Vorontsovskoe gold deposit (Northern Urals). Mineralogy 8:5–93

Laznicka P (2010) Giant metallic deposits: future sources of industrial metals, 2nd edn. Springer-Verlag, Berlin Heidelberg, p 826

Lin J, Yin M, Wang J, Liu J, Tsang DCW, Wang Y, Lin M, Li H, Zhou Y, Song G, Chen Y (2020) Geochemical fractionation of thallium in contaminated soils near a large-scale Hg-Tl mineralized area. Chemosphere 239:124775

Lottermoser BG (2010) Mine wastes: characterization, treatment and environmental impacts, 3rd edn. Springer, Berlin, p 400

Lottermoser BG (2017) Predictive environmental indicators in metal mining. In: Environmental indicators in metal mining, pp 3–12, Springer: Berlin/Heidelberg, Germany

Majzlan J, Drahota P, Filippi M (2014) Paragenesis and crystal chemistry of arsenic minerals. Rev Mineral Geochem 79:17–184

Majzlan J, Haase P, Plášil J, Dachs E (2019) Synthesis and stability of some members of the pharmacosiderite group, $AFe_4(OH)_4(AsO_4)_3 \cdot nH_2O$ (A= K, Na, 0.5Ba, 0.5Sr). Can Mineral 57:663–675

Manceau A, Simionovic AS, Findling N, Glatzel P, Detlefs B, Wegorzewski AV, Mizell K, Hein JR, Koschinsky A (2022) Crystal chemistry of thallium in marine ferromanganese deposits. ACS Earth Space Chem 6:1269–1285

Martin LA, Wissocq A, Benedetti MF, Latrille C (2018) Thallium (Tl) sorption onto illite and smectite: Implications for Tl mobility in the environment. Geochim Cosmochim Acta 230:1–16

Mills SJ, Kampf AR, Williams PA, Leverett P, Poirier G, Raudsepp M, Francis CA (2010a) Hydroniumpharmacosiderite, a new member of the pharmacosiderite supergroup from Cornwall, UK: structure and description. Mineral Mag 74:863–869

Mills SJ, Hager SL, Leverett P, Williams PA, Raudsepp M (2010b) The structure of H_3O^+-exchanged pharmacosiderite. Mineral Mag 74:487–492

Mills SJ, Rumsey MS, Favreu G, Spratt J, Raudsepp M, Dini M (2011) Bariopharmacoalumite, a new mineral species from Cap Garonne, France and Mina Grande, Chile. Mineral Mag 75:135–144

Mills SJ, Petrini E, Bellatreccia F, Schlüter J, Kampf A, Rumsey M, Dini M, Spratt J (2013) Caesiumpharmacosiderite, IMA 2013–096. CNMNC Newsletter No. 18, December 2013, page 3257. Mineral Mag 77:3249–3258

Mills SJ, Meisser N, Rumsey MS, Hay DG, Spratt J, Ansermet S, Vonlanthen P (2014) Strontiopharmacosiderite, IMA 2013–101. CNMNC Newsletter No. 19, February 2014, page 166. Mineral Mag 78:165–170

Momma K, Izumi F (2011) VESTA 3 for three-dimensional visualization of crystal, volumetric and morphology data. J Appl Crystallogr 44:1272–1276

Morin G, Lecocq D, Juillot F, Calas G, Ildefonse P, Belin S, Briois V, Dillmann P, Chevallier P, Gauthier C, Sole A, Petit PE, Borensztajn S (2002) EXAFS evidence of sorbed arsenic(V) and pharmacosiderite in a soil overlying the Echassières geochemical anomaly, Allier, France. Bull Soc Géolog France Société Géologique De France 173:281–291

Nonius (2005-2007) COLLECT data collection software. 2005–2007 Nonius BV, Delft, The Netherlands

Otwinowski Z, Borek D, Majewski W, Minor W (2003) Multiparametric scaling of diffraction intensities. Acta Crystallogr A 59:228–234

Parsons S, Flack HD, Wagner T (2013) Use of intensity quotients and differences in absolute structure refinement. Acta Crystallogr B 69:249–259

Rodríguez-Mercado JJ, Álvarez-Barrera L, Mateos-Nava RA, Rodríguez-Espitia JD, Altamirano-Lozano MA (2019) Induction of cytotoxicity in human cells exposed to thallium(I) and thallium(III). Curr Top Toxicol 15:17–27

Rumsey MS, Mills SJ, Spratt J (2010) Natropharmacoalumite, $NaAl_4[(OH)_4(AsO_4)_3] \cdot 4H_2O$, a new mineral of the pharmacosiderite supergroup and the renaming of aluminopharmacosiderite to pharmacoalumite. Mineral Mag 74:929–936

Rumsey MS, Mills SJ, Spratt J, Hay DG, Farber G (2014) Thallium-pharmacosiderite, IMA 2013–124. CNMNC Newsletter No. 20, June 2014, page 553. Mineral Mag 78:549–558

Schmetzer K, Horn W, Bank H (1981) Alumopharmakosiderit, $K[Al_4(OH)_4(AsO_4)_3] \cdot 6.5H_2O$, ein neues Mineral. N Jahrb Mineral Mh 1981:97–102

Shannon RD (1976) Revised effective ionic radii and systematic studies of interatomic distances in halides and chalcogenides. Acta Crystallogr A 32:751–767

Sheldrick GM (2015a) SHELXT – Integrated space-group and crystal structure determination. Acta Crystallogr A 71:3–8

Sheldrick GM (2015b) Crystal structure refinement with SHELXL. Acta Crystallogr C 71:3–8

Steinfeld A, Đorđević T, Kolitsch U, Nagl P, Tasev G, Serafimovski T, Boev I, Boev B (2021) An update on secondary thallium minerals. Mitt Österr Mineral Ges 167:145

Van Aken P, Liebscher B (2002) Quantification of ferrous/ferric ratios in minerals: new evaluation schemes of Fe L23 electron energy-loss near-edge spectra. Phys Chem Mineral 29:188–200

Vaněk A, Chrastný V, Mihaljevič M, Drahota P, Grygar T, Komárek M (2009) Lithogenic thallium behaviour in soils with different land use. J Geochem Explor 102:7–12

Vaněk A, Komárek M, Vorkurková P, Mihaljevič M, Šebek O, Panušková G, Chrastný V, Drábek O (2011) Effect of illite and birnessite on thallium retention and bioavailability in contaminated soils. J Hazard Mater 191:170–176

Vaněk A, Grösslová Z, Mihaljevič M, Ettler V, Trubač J, Chrastný V, Penížek V, Teper L, Cabala J, Voegelin A, Zádorová T, Oborná V, Drábek O, Holubík O, Houška J, Pavlů L, Ash C (2018) Thallium isotopes in metallurgical wastes/ contaminated soils: a novel tool to trace metal source and behavior. J Hazard Mater 343:78–85

Vaněk A, Vejvodová K, Mihaljevič M, Ettler V, Trubač J, Vaňková M, Goliáš V, Teper L, Sutkowska K, Vokurková P, Penížek V, Zádorová T, Drábek O (2021) Thallium and lead variations in a contaminated peatland: A combined isotopic study from a mining/ smelting area. Environ Poll 290:117973–117982

Vaněk A, Vejvodová K, Mihaljevič M, Ettler V, Trubač J, Vaňková M, Teper L, Cabala J, Sutkowska K, Voegelin A, Göttlicher J, Holubík O, Vokurková P, Pavlů L, Galušková I, Zádorová T (2022) Evaluation of thallium isotopic fractionation during the metallurgical processing of sulphides: an update. J Hazard Mater 424:127325–127332

Vignola P, Rotiroti N, Hatert F, Dal Bo F, Gentile P, Albertini C, Merlini M, Risplendente A, Pavese A (2018) Plumbopharmacosiderite, $Pb_{0.5}Fe^{3+}_4[(OH)_4(AsO_4)_3] \cdot 5H_2O$, a new mineral species from the Monte Falò Pb-Zn mine near the village of Coiromonte in the Armeno municipality, Novara Province, Italy. Can Mineral 56:143–150

Voegelin A, Pfenninger N, Petrikis J, Majzlan J, Plötze M, Senn A-C, Mangold S, Steininger R, Göttlicher J (2015) Thallium speciation and extractability in a thallium- and arsenic-rich soil developed from mineralized carbonate rock. Environ Sci Technol 49:5390–5398

Voegelin A, Wick S, Pfenninger N, Mangold S, Baeyens B, Marques Fernandes M (2022) Thallium adsorption onto phyllosilicate minerals. Environ Sci Processes Impacts 24:1343–1350

Voudouris P, Kati M, Magganas A, Keith M, Valsami-Jones E, Haase K, Klemd R, Nestmeyer M (2021) Arsenian pyrite and cinnabar from active submarine nearshore vents. Paleochori Bay, Milos Island, Greece. Minerals 11:1–25

Warr LN (2021) IMA-CNMNC approved symbols. Mineral Mag 85:291–320

Wick S, Baeyens B, Marques Fernandes M, Voegelin A (2018) Thallium adsorption onto illite. Environ Sci Technol 5:571–580

Wick S, Peña J, Voegelin A (2019) Thallium sorption onto manganese oxides. Environ Sci Technol 53:13168–13178

Wick S, Baeyens B, Marques Fernandes M, Göttlicher J, Fischer M, Pfenninger N, Plötze M, Voegelin A (2020) Thallium sorption and speciation in soils: Role of micaceous clay minerals and manganese oxides. Geochim Cosmochim Acta 288:83–100

Willner J, Fornalczyk A, Jablonska-Czapla M, Grygoyc K, Rachwal M (2021) Studies on the content of selected technology critical elements (Germanium, Tellurium and Thallium) in electronic waste. Materials 14:3722–3737

Zhou TF, Fan Y, Yuan F, Wu MA, Hou MJ, Voicu G, Hu QH, Zhang QM, Yue SC (2005) A preliminary geological and geochemical study of the Xiangquan thallium deposit, eastern China: the world's first thallium-only mine. Mineral Petrol 85:243–251